

# A study on Performance Boost of a 17 m class Cherenkov telescope with a SiPM-based camera

Cornelia Arcaro<sup>1 †</sup>, Michele Doro<sup>1,2 †</sup>, Julian Sitarek<sup>3 †</sup>, Dominik Baack<sup>4</sup>,

<sup>1</sup> *Istituto Nazionale di Fisica Nucleare (INFN) sez. Padova, via Marzolo 8, I-35131, Padova (Italy)*

<sup>2</sup> *University of Padova, Department of Physics and Astronomy, via Marzolo 8, I-35131, Padova (Italy)*

<sup>3</sup> *University of Lodz, Faculty of Physics and Applied Informatics, Department of Astrophysics, 90-236 Lodz, Poland*

<sup>4</sup> *Technische Universität Dortmund, D-44221 Dortmund, Germany*

† *Correspondence: cornelia.arcaro@pd.infn.it, michele.doro@unipd.it, jsitarek@uni.lodz.pl*

arXiv:2212.09456v2 [astro-ph.IM] 19 Sep 2023

---

## Abstract

The current generation of Imaging Atmospheric Cherenkov Telescopes (IACTs), comprised of major installations such as the MAGIC, H.E.S.S. and VERITAS telescopes, is sometimes called the 3<sup>rd</sup> generation of such instruments. These telescopes use multipixel cameras composed of hundreds up to thousands photomultiplier tubes (PMTs). The supremacy of PMTs is currently being challenged by photon sensors, rapidly spreading in popularity: the silicon photomultipliers (SiPMs), that are becoming a valid alternative thanks to their high PDE, low operating voltage and flexibility in installation. In this report, we investigate the performance of an existing 3<sup>rd</sup> generation IACT array (taking as a working example MAGIC), in which PMTs would be replaced with SiPMs, applying generalized simulations, not tuned for a specific hardware solution. We find an energy-dependent improvement in sensitivity, reaching a factor of three at the current trigger threshold energy. Interestingly, we also find that the stronger sensitivity of SiPMs in the red part of the spectrum, a source of background for IACTs, does not affect this performance.

*Keywords:* IACT, MAGIC, PMT, SiPM

---

## 1. Introduction

Imaging Atmospheric Cherenkov Telescopes (IACTs) detect the Cherenkov light radiated in Extensive Atmospheric Showers (EASs) in the Earth's atmosphere at the height of 10-20 km a.s.l [1, 2]. EASs are produced by energetic cosmic rays or gamma rays impinging the Earth. The Cherenkov radiation is peaked in the blue-UV, has a duration of few nanoseconds, and illuminates an area of few tens of thousands square meters at ground level, depending on the energy of the primary particle. The observations can only be performed at moonless nights or nights with moderate moonlight and are made through telescopes with large light collectors. However, in recent times, technical solutions were implemented to operate also with stronger and stronger moon levels, selecting targets at a sufficient angular distance from the Moon [see, e.g., 3, 4]. For concreteness, we base our study on a specific 3<sup>rd</sup> generation IACT system, the Major Atmospheric Gamma-ray Imaging Cherenkov (MAGIC) telescopes, operating since 2003 at the Observatorio Roque de Los Muchachos (ORM) on the island of La Palma. In Sec. 7, we discuss about the applicability of these results for other installations. Each of the two MAGIC telescopes has a 17 m-diameter ( $f$ -number= 1) parabolic reflector, tessellated with about 250 mirror facets [5]. To catch the brief Cherenkov light flashes, the MAGIC telescopes are equipped with two identical cameras, each composed of 1039 photomultiplier tubes (PMTs). The PMTs are organised in 265 clusters of 7 photodetectors each, assembled in modules that can easily be

plugged in or out independently from each other. It is therefore possible, to separately remove a module, and replace it with a different one, provided the front- and back-end electronic is compatible. The MAGIC PMTs are Hamamatsu R10408 6-dynodes with an hemispherical bi-alkali cathode of 1' diameter, operated at a voltage of  $\approx 1$  kV. Each PMT is equipped with a compound parabolic concentrator adapted from the design of the so-called Winston cone [6, 7], that reduces the dead area between neighbouring PMTs and avoids the stray-light coming from far-off the mirror dish. Silicon Photomultipliers (SiPMs) are photosensors composed of microscopic diode cells assembled in matrices of thousands, to reach sizes of few mm across, discussed in more details in Sec. 2. They are currently replacing PMTs where compactness is required and because they operate at low voltage. These devices are advancing rapidly in the field of fast photodetectors. Compared to PMTs, besides their low operating voltage, they provide advantages such high efficiencies, insensitivity to magnetic fields, and robustness against bright ambient light. The compact geometrical size of SiPMs allow to easily arrange them, but makes it complicate to cover large areas such as those of IACT cameras, of the order of two square meter. Other drawbacks compared to Cherenkov applications of PMTs are the optical crosstalk between adjacent cells and the larger sensitivity to red light, as well as a higher dark current. Normally multiple SiPMs must be combined together to match the sensitive area of a PMT, in this case, also the signal summation could provide larger time-spread signal than that of PMTs. Currently, the development and testing of SiPM-based

modules in the MAGIC cameras is ongoing in preparation of a possible camera upgrade for MAGIC or the future Cherenkov Telescope Array [8]. Furthermore, SiPMs are currently already adopted as main photosensors in some telescope designs for the Cherenkov Telescope Array (CTA) [9, 10, 11]. This solution is valid especially in the case of a double-optics Schwarzschild-Couder design in which a secondary mirror not only counteracts some geometrical aberrations, but also allows for a reduction of the camera occupancy and therefore the size of its pixels [12]. There are also studies to equip single-optics Davies-Cotton or parabolic CTA telescopes with SiPMs, but so far only the technological feasibility is under evaluation [13, 14, 15, 16].

It is therefore interesting to evaluate the expected performance of the 3<sup>rd</sup>-generation IACTs with SiPM-based cameras. However, a complete estimation of the validity of a SiPM-equipped camera for this generation of telescopes is out of the scope of this paper. This would require a) comparing selected replacement of photosensors and electronics to a complete new assembly of the camera b) evaluating in details the grouping of SiPMs into single pixels, c) using specifically developed SiPMs after bidding with companies, as well as several other aspects, not excluding the related cost and scientific opportunity. In this work, we focus on a ‘minimal hardware change’ scenario, in which we replaced the MAGIC PMT modules with clusters of SiPMs, leaving the rest of the system untouched. This approach allows us to give a valuable input for the expected performance of a new SiPM-based camera.

The paper is structured as follows: In Sec. 2 we discuss the focal-plane photosensors, the current generation PMTs and SiPMs, comparing their performance. In Sec. 3 we review the factors that affect the light yield of the camera, especially considering how the original spectral distribution of the Cherenkov light is modified through the detection by the instrument. In Sec. 4 we compute the light yield for the case of PMTs and SiPMs. We also discuss the possibility to filter out the red part of the spectrum with a dedicated dichroic window in front of the camera. The details of the SiPM camera simulations are presented in Sec. 5. The performance with a SiPM-based camera is discussed in Sec. 6. In Sec. 7 we discuss the technical feasibility of a potential camera upgrade and the accuracy of our results. We summarise and conclude in Sec. 8.

## 2. Focal plane photosensors

SiPMs are grids of Single Photon Avalanche photoDiodes (SPADs) on silicon substrate [17]. Each SPAD is a microscopic independent Avalanche PhotoDiodes (APDs), operated in Geiger-mode, i.e., counting single photons. However, when combining thousands of microcells, the dynamic range of a SiPM can go from a single to thousands of photons for each square millimeter. The SiPM matrix wafer is prepared during the initial production and later wired and assembled. The thickness of the sensor is of the order of one millimeter, making the detector very compact. SiPMs are operated at bias voltage of few tens of volts, carefully set to provide optimal performance in terms of single photon response, linearity, and current noise.

The small size also makes SiPMs insensitive to regular ambient magnetic fields.

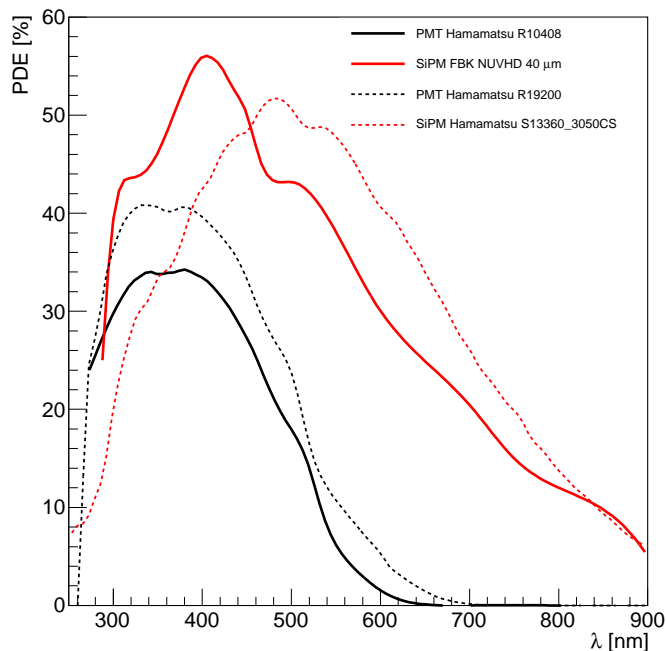


Figure 1: PDE curves for the reference PMTs and SiPMs for this paper. The current MAGIC PMT is a Hamamatsu R10408 mounted in the MAGIC cameras (black solid curve [18]). The solid red curve displays the FBK NUVHD3 40  $\mu$  sensor [19]. These two are used in this work. For further comparison, the dotted red curve displays the SiPM S13360 from Hamamatsu [20] and the dotted black curve reports the CTA LST-1 PMT of type Hamamatsu R19200 [21].

In Fig. 1, we compare the photo detection efficiency (PDE) of one benchmark PMT Hamamatsu R10408 [18], currently installed in MAGIC, the PMTs Hamamatsu R19200 [21], currently installed in the first CTA large-size telescope prototype (LST-1) and two benchmark SiPMs that are under scrutiny for the use in CTA cameras. The SiPMs are a commercial Hamamatsu S13360<sup>1</sup> [20] and a NUVHD3 sensor by Fondazione Bruno Kessler (FBK) [19, 22]. As one can see, the SiPMs have a peak PDE in a part of the spectrum at significantly larger wavelengths than that of the PMTs. They also feature a good efficiency in the red part of the spectrum where PMTs are usually less sensitive.

In the following, we take the FBK NUVHD3 photosensor as a case example. This is a precursor of a class of SiPMs under constant development. For example, the CTA small-size telescope prototype [23] mounts version NUVHD6 of this sensor, however with performance not dissimilar to the NUVHD3 considered here [22]. The SiPM development is mostly focused on the reduction of dark noise and optical cross-talk.

One significant source of noise for SiPMs is the optical crosstalk generated by secondary photons created during the charge recombination. Such spurious photons may trigger secondary breakdowns in neighboring cells [24]. The effect is a randomized enhancement of the amplitude of the measured signal. This effect can be reduced with specific design geometry

<sup>1</sup>Datasheet at [https://www.hamamatsu.com/resources/pdf/ssd/s13360\\_seri](https://www.hamamatsu.com/resources/pdf/ssd/s13360_seri)

such as building trenches among neighboring cells [22]. Also the use of light-guides in front of SiPM allows to reduce this effect because spurious photons are not reflected back to the sensor but are free to escape outward [25]. The irreducible optical cross-talk must be modeled during signal reconstruction. However, the SiPMs main drawback with respect to PMTs remains their reduced size, which cannot exceed 1-2 cm<sup>2</sup> with current technologies, due to the large capacitance generated by the compact geometry. In case a large sensitive area must be covered (as that of the focal plane of an IACT, of the order of 2 m<sup>2</sup>), particular solutions must be adopted. These are: a) the positioning of optical funnels, in the form of either hollow or solid concentrator<sup>2</sup> at the entrance of the individual SiPMs, that increase the sensitive area by guiding the light to the photosensor surface, e.g. as done by Huber et al. [26], Aguilar et al. [27] or b) the combination of a number of photosensors into one larger pixel via summation, possibly also combined with a light funnel [13, 28], to avoid a too large number of channels.

An example of a telescope using solid-state photosensors is that of the First G-APD Cherenkov Telescope (FACT) [29]. The FACT telescope is a single-dish 4 m-diameter telescope located at the MAGIC site, built upgrading a decommissioned HEGRA telescope and successfully operative for about a decade. FACT has successfully operated for several years a Geiger-mode avalanche photodiode camera described by Biland et al. [29]. G-APD photosensors allows FACT to routinely operate even under strong moon level [30] allowing for a duty cycle increase of 30% [31]. MAGIC is currently hosting four SiPM clusters at the edges of the camera. They are only test installations not used for regular data analysis. One of the clusters hosts seven and the other nine 6 × 6 mm<sup>2</sup> photosensors per pixel. These are read out with the standard MAGIC data acquisition system [13, 28, 8].

Even while we do not aim at a full simulation of a specific hardware solutions, in order to make the assessment of performance realistic, we adjusted a number of parameters related to SiPMs in the Monte Carlo simulation and analysis. This is presented in Sec. 5.

### 3. Differential light yield at the photosensors

Considering the difference in PDE between PMTs and SiPMs is wavelength-dependent, it is important to also spectrally characterise the light impinging the photosensors. There are several effects that affect the spectrum hitting the camera pixels: first, the Cherenkov spectrum at ground, that may non trivially change in function of the intrinsic energy of the primary particle, the particle type, and the altitude above the horizon (or the zenith angle ZA or zenith distance ZD). In principle, different atmospheric conditions can affect as well the Cherenkov light extinction in a wavelength-dependent way. This effect is less general to model and it is less severe. Other factors are the reflectivity of the mirror facets, the transmissivity of the eventual

<sup>2</sup>The classical shape of such funnel is the compound parabolic concentrator described in [6, 7]

entrance window (in the case of MAGIC made of a plexiglass sheet, see later), and the spectral properties of the light concentrators. All these factors contribute to shaping the wavelength-dependent light yield at an IACT camera.

#### 3.1. Cherenkov light yield from gamma-ray and cosmic-ray induced atmospheric showers

The Cherenkov spectra at ground studied for this work are obtained from dedicated Monte Carlo simulations. These are based on a customised version of the publicly available software for simulations of air showers, dubbed Corsika (COsmic Ray SIMulations for KASCADE), which is used within the MAGIC collaboration [32]. To model the light extinction in the atmosphere, we used an atmospheric model specifically produced for the sky at the ORM [33]. We simulated 180,000 gamma ray events and 60,000 proton events in total, at different impact parameters to simulate a realistic condition. To evaluate the effect of the sky position and primary energy on the impinging Cherenkov spectrum, we considered three incident angles (5, 45, 65°) and three energies for gamma rays: 60, 400, 1500 GeV and an energy of 180 GeV for protons<sup>3</sup>. This corresponds to 20,000 simulated events per set.

At the emission point, the Cherenkov yield is generated with a  $\lambda^{-2}$  spectrum [34]. This spectrum is attenuated with strong chromaticity by the atmosphere molecular content. At short wavelengths, ozone plays the major role. At longer wavelengths, Rayleigh scattering with Nitrogen and Oxygen becomes the strongest attenuating agent. IACTs are typically located in very clean and dry atmospheric environments, whereas the conditions are practically those of free troposphere, with the aerosol content playing a significant role only in non-optimal atmospheric conditions [35].

Fig. 2 shows the simulated Cherenkov spectra at the focal plane for primary gamma rays and protons at different energies and zenith angles. The spectrum is in arbitrary units and consider only the atmospheric absorption. No other wavelength-dependent effects, e.g. the mirror reflectivity, are considered. The curves are obtained by summing over all the events in a batch that give a detectable number of photons. This varies significantly event by event even with the same settings, due to the stochasticity of the EAS development and the simulation. For each spectrum, the peak position is identified as the average of the three highest points of the curve<sup>4</sup>. The peak positions are reported in Table 1.

From Fig. 2 one can see that with increasing incident angle of the primary particle, the absolute photon yield from EASs decreases significantly. This is due to the increased air mass

<sup>3</sup>Considering protons produce copious pions in hadronic interactions, electromagnetic subshowers are initiated by a charged particle with roughly one third of the primary proton energy, hence the factor of three in energy in comparison between primary gamma rays and protons

<sup>4</sup>For this reason, the statistical uncertainty on the peak position cannot be computed. Instead, the sample was split into two subsets to check the reproducibility of the peak position. For simulations at 5 and 45 deg zenith angle we found no difference. Only in the case of simulations with a zenith angle of 65 deg, the peak position was shifted by a few nm, probably due to the flatter maximum in the spectra.

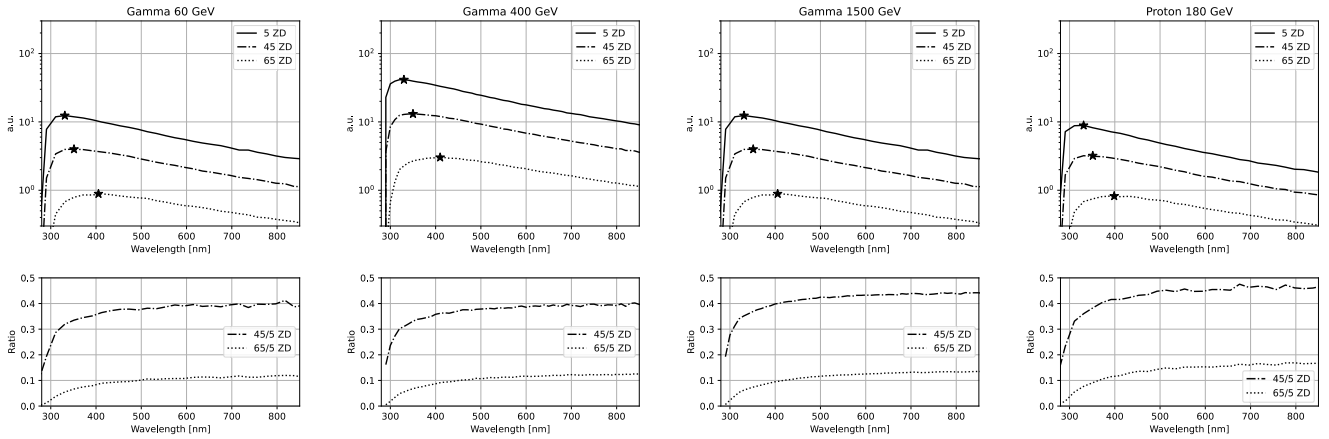


Figure 2: Cherenkov spectrum at the focal plane, in function of the energy and incoming direction of incident gamma rays (three leftmost columns) and incident protons (rightmost column), considering only atmospheric absorption (e.g. not the mirror reflectivity loss). The top row reports the total number of photons in arbitrary units in the standard MAGIC cameras for three different energies for primary gamma rays: 60 GeV (left), 400 GeV (center-left) and 1500 GeV (center-right) and for the energy of 180 GeV for protons. In each pad, three incident zenith angles are reported: 5° (solid line), 45° (long-dashed line) and 65° (short-dashed line). The bottom row shows the ratio of the individual spectra simulated for higher zenith angles with respect to the 5° case. The black stars on the plots indicate the peak of Cherenkov spectra. The corresponding numerical values are reported in Table 1.

Cherenkov spectra peak wavelength			
	5°	45°	65°
$\gamma$ 60 GeV	331 nm	351 nm	405 nm
$\gamma$ 400 GeV	330 nm	350 nm	410 nm
$\gamma$ 1500 GeV	330 nm	340 nm	403 nm
$p$ 180 GeV	331 nm	351 nm	398 nm

Table 1: Position of the maximum of the Cherenkov spectrum at ground as a function of the energy (rows) and incident angle of the primary gamma ray (columns). Statistical uncertainties cannot be accurately computed as discussed in the text and are not reported.

the Cherenkov light travels through before reaching the ground, which results in higher extinction. A second effect is that the position of the maximum of the Cherenkov spectrum moves to longer wavelengths (redshift) with increasing incident angle of the gamma ray. This is due to the differential extinction of the atmosphere at different wavelengths (Rayleigh scattering). The maximum becomes significantly redshifted with increasing incident angle, up to 20% between 5° and 65°, but almost independently of the energy of the gamma ray. This behavior is especially interesting in the context of observation at large zenith angles (above 75°) which are currently being carried out in the field [see, e.g. 36]. The insignificant energy dependence of the Cherenkov peak allows us to neglect any energy-dependent effect for the computation of the photon yield in the remainder of this work. We will revisit the energy dependence during the examination of the interplay with the night sky background (Sec. 3.2) and the overall instrument sensitivity (Sec. 6).

It is also interesting to compare the Cherenkov spectrum emitted by electromagnetic showers and hadronic (sub)showers. In Fig. 2 (rightmost column) we report the Cherenkov spectra from electromagnetic subshowers generated by 180 GeV protons. The trend of the maximum Cherenkov radiation shifting to longer wavelengths and decreasing with increasing inclina-

tion of the primary particle shows the same regularity between gamma ray and proton induced atmospheric showers.

### 3.2. The light of the night sky

IACTs operate in the presence of the optical background from the Light Of the Night Sky (LONS). The LONS is composed of starlight, zodiacal light and airglow. The LONS is strongly site dependent and also strongly vary with the time of the year, zenith angle and moon phases, among other things. For an IACT, it constitutes the so-called Night Sky Background (NSB).

Fig. 3 shows a typical NSB at the ORM obtained from data from Benn and Ellison [37] and converted for a pixel size of MAGIC. There are two major differences between the NSB and Cherenkov spectrum: a) the NSB *increases* with the wavelength and is concentrated at the red and infrared part of the spectrum, and b) the NSB shows several very prominent *peaks* over the steadily increasing background. This is directly related to the emission spectrum of the air-glow. In reality, this is an average picture, as discussed above.

Having the pixels of an IACT camera hit by spurious photons creates two problems: a) fake triggers up to saturation of the data acquisition system and b) noise within the signal with a consequent deterioration of the signal-to-noise ratio (SNR). We have already discussed that SiPMs are more sensitive than PMTs in the red part of the spectrum (see Fig. 1). It will be therefore important to weigh this effect properly.

### 3.3. Other optical elements affecting the light yield

A number of optical elements of IACTs exhibit wavelength-dependent behaviour, in particular the mirror dish facets, the light concentrators attached to the camera pixels and the plexiglass entrance window. The switch to a SiPM-based camera would not require modifications of these aspects but nevertheless, their wavelength-dependency still needs to be considered

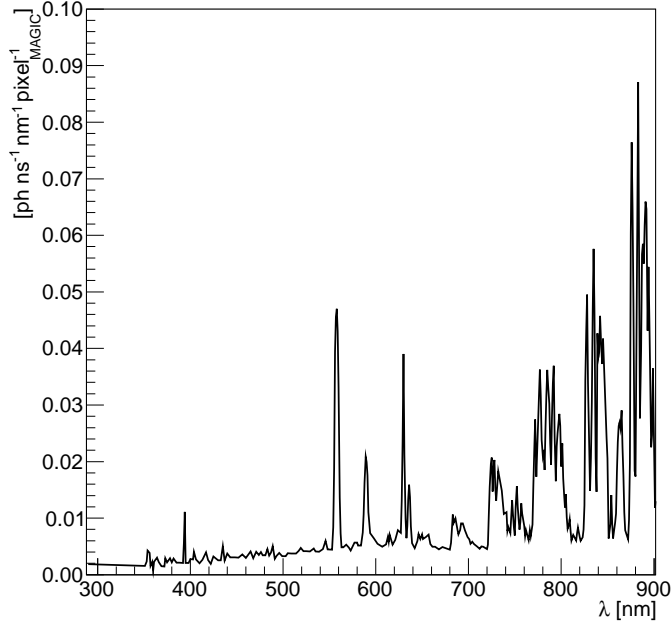


Figure 3: The spectrum of the NSB at La Palma. The data are taken from Benn and Ellison [37] and converted to number of photons reaching one MAGIC pixel in one nanosecond.

in this study, as the optics might affect the relevance of the PDE of the SiPM at different wavelengths. We pay special attention to the camera entrance protection window (see Sec. 3.3.1), whose wavelength-dependent transmission can provide a cost-effective way to improve the performance of a SiPM-based camera, as we will see later.

**Mirrors.** The mirrors of the MAGIC telescopes (see [5, 38, 39]) have a specific spectral reflectivity, that depends on the material used for the mirror surface. Their reflectance is achieved by an aluminium alloy, varying between different mirror designs, coated with a protective quartz layer. The thickness of this layer affects the position of the maximum spectral reflectivity. Fig. 4 shows the spectral reflectivity of a typical MAGIC mirror [40].

**Light funnels.** The cathodes of the photosensors in the current MAGIC cameras are hemispherical, causing some dead area between neighbouring pixels. Light concentrators, often called “Winston cones” [6, 7, 41], reduce the size of this area. At the same time they reduce the number of NSB photons entering at large field angles, increasing the SNR for the faint gamma-induced signal. In MAGIC, the light guide is made of a few cm high ultra-thin metallized foil shaped into a parabolic geometry with a larger hexagonal entrance and a smaller circular exit, which is directly attached to the cathode of the PMT. The light concentrators are made from a plastic material with aluminised Mylar foil of about 95% reflectivity above 300 nm [42]. Fig. 4 shows the spectral reflectivity of this foil for light incident at  $30^\circ$ <sup>5</sup>. This contribution is neglected for the light yield compar-

ison study in Sec. 4, but it is fully considered for the study of performance in Sec. 5 and Sec. 6.

### 3.3.1. Camera protection window

To protect the pixels and electronic from environmental conditions, the focal plane instrumentation of MAGIC is hosted in a thermally regulated, water- and light-tight container. A transparent plexiglass window (or similar polymethyl methacrylate-like materials; PMMA) is used to seal it, while proving good light transmission, specially close to the maximum of the Cherenkov spectrum. As a further protection, the plexiglass window and the camera is closed by light- and water-insulating lids, closed during the day. The plexiglass window in front of the MAGIC camera is of kind Plexiglas® GS Clear 2458 SC. It has a transmission of 92% at all wavelengths above 355 nm, which is slowly decreasing to 88% at 300 nm with a sharp cut-off at 280 nm (see Fig. 4). As there is no sizable effect on the wavelength range of interest, as such, we can exclude this contribution for the spectral-response comparison between PMT and SiPM for the light yield comparison study in Sec. 4 but this contribution is considered when performing the full telescope simulation of Sec. 5 and Sec. 6.

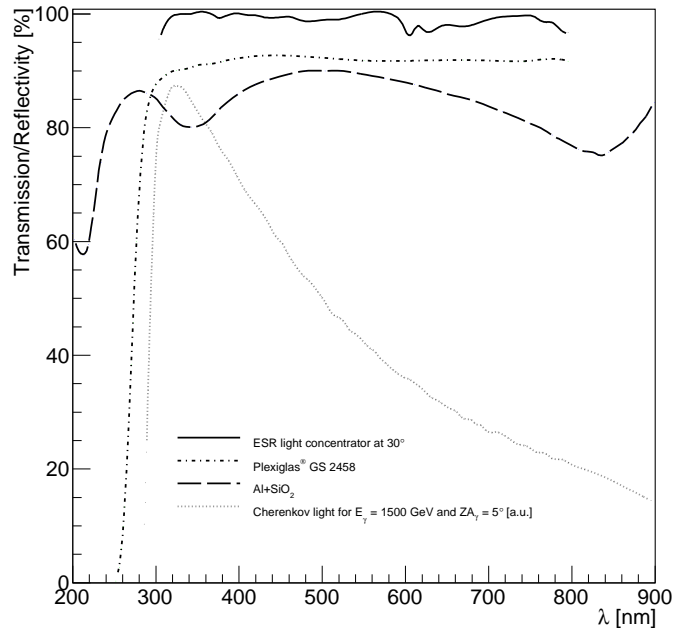


Figure 4: Transmission of the PMMA of type Plexiglas®GS Clear 2458 SC (dashed-dotted black line) and spectral reflectivity of the enhanced specular-reflector light concentrator foil [42] at  $30^\circ$  incidence (solid black line) and of the quartz-coated all-aluminium MAGIC mirrors (long-dashed, [40]). The Cherenkov spectrum produced by a 1500-GeV gamma ray with  $5^\circ$  incident angle is shown for reference (dotted grey line).

## 4. Light yield with a SiPM-based camera

We now move to combine all the spectral-dependent factors described in the previous section to understand how these affect the detection of Cherenkov light from primary gamma-ray

<sup>5</sup>The reflectivity depends slightly on the inclination angle.

induced EASs as well as the noise by the NSB. We do this in [Sec. 4.1](#). Given the effect of the sensitivity of the SiPM to the red band and therefore to the NSB, we discuss a possible alternative technical solution to counteract this effect in [Sec. 4.2](#).

#### 4.1. Cherenkov light and NSB yield

[Fig. 5](#) (left) shows the Cherenkov signal yield that survives the reflection onto the mirror dish of the MAGIC telescope and the subsequent detection in a camera pixel, either consisting of a conventional PMT or the specific FBK SiPM considered in this study. We limit our considerations to the case of a primary gamma ray of 1500 GeV, having shown that the amount of Cherenkov light at the ground simply scales linearly with primary energy, but the spectrum is not changed (see [Sec. 4](#)). The wavelength-independent effects of the camera window and the light guides are also here excluded. Already a quick inspection of the figures shows that the use of a SiPM strongly increases the signal in the blue part of the spectrum, allowing to gather more Cherenkov photons, but also makes the instrument more sensitive in the red part above 500 nm. A more quantitative comparison of [Fig. 5](#) is made in [Table 2](#) (first rows, column "SiPM / PMT") in which we report the fractional increase of the integrals of the spectra displayed in [Fig. 5](#) for the SiPM and PMT case<sup>6</sup>. In all cases, the SiPM provides a significant boost in light yield with respect to the PMT: the total photon yield increases from a factor 2.2 to 2.5 going from 5 to 65° incident angle of the primary particle. This increase with the incident angle is due to the redshift of the maximum of the Cherenkov spectrum as the Rayleigh absorption increases (see [Sec. 3.1](#)).

yield	SiPM / PMT	(SiPM+w) / PMT
Cherenkov Light		
$ZA_\gamma = 5^\circ$	2.20	1.76
$ZA_\gamma = 45^\circ$	2.28	1.76
$ZA_\gamma = 65^\circ$	2.52	1.84
Night Sky Background		
	5.30	1.66

Table 2: Fractional increase of Cherenkov photons produced by a primary gamma ray of 1500 GeV impinging at different zenith angles, as well as the increase of the NSB photons detected by a SiPM with respect to a PMT. The ratio is also reported for a technical solution applied to suppress/eliminate the sensitivity of the SiPM to the red band of the spectrum, which is based on the use of a low-pass filter ("SiPM+w").

The detection efficiency of the Cherenkov signal is not the only factor influencing the sensitivity of an IACT, because of the interplay with the NSB ([Sec. 3.2](#)). The effect of SiPM and PMT on the NSB light yield is also shown in [Fig. 5](#) (right). A visual inspection clearly shows that the behavior in the case of PMTs and SiPMs is rather different: while in the former case, above 650 nm, the NSB does not contribute significantly to the background light level of each camera pixel, instead in the SiPM case, it does. Second, the contribution of spectral

<sup>6</sup>For reasons already expressed in [Sec. 3.1](#), we cannot compute the statistical uncertainties of these values.

peaks present in the NSB changes in the two cases: in the PMT case mostly the 557.7 nm peak is detected, while in the SiPM case, many other significant peaks of the NSB contribute to the background level in the camera pixels. Looking again at [Table 2](#) (bottom row, column "SiPM / PMT"), we quantify the increased number of photons with a factor of 5.3 when using SiPMs instead of PMTs. These results are in line with those reported in [\[8\]](#).

We asked ourselves whether such an additional "red" contribution could be avoided. This is in principle achievable in different ways: a) it is possible to realize a primary mirror with dichroic properties. For example Förster et al. [\[43\]](#) demonstrated that multilayer dielectric mirrors could achieve this goal. We discarded this option for MAGIC, as replacing the entire reflectors is hardly feasible cost-wise b) another possibility is that of replacing the camera window (see [Sec. 3.3.1](#)) with a dichroic plexiglass cutting the light above a certain wavelength. This is the topic of the next [Sec. 4.2](#), c) finally, in principle one could also operate at the photon detector context and e.g. reduce the efficiency or the transmittance in the red part by special coatings<sup>7</sup>. This technical solution is not investigated here further. All in all, the effect of the three solutions would be similar: the light yield in the red part would be reduced. The anticipated impact of such solutions on the fraction increase of photons is reported in [Table 2](#), column "SiPM+w / PMT". One can see how such filtering effect has a moderate impact on the Cherenkov light yield, but a stronger one on the NSB, with relative weights similar as in the case of PMTs.

#### 4.2. A technical solution to reduce the photon yield of the red light

From [Fig. 5](#), it clearly emerges that if one could somehow cut out the sensitivity of SiPMs to the red part of the spectrum, the background light level due to the NSB could be reduced. Such a possibility may be offered, e.g., by substituting the neutral plexiglass window ([Sec. 3.3.1](#)) with a dichroic camera window that would filter the dominant red part of the NSB spectrum by reflection or absorption. The modification of the entrance of the camera of IACTs is not a novelty in the field. It is used routinely in MAGIC during strong moonlight observations where a second protective camera window is mounted in front of the existing one [\[3\]](#). A similar solution was developed in VERITAS [\[4\]](#). We will discuss the technical feasibility of this solution in [Sec. 7](#). Here we show how to optimize the cut-off wavelength  $\lambda_{\text{cut}}$ .

To evaluate if the effect of the increased NSB level detected with SiPMs can be mitigated with a filter, we have performed a dedicated study taking into account the wavelength-dependent reflectivity of the MAGIC mirrors and the PDE of the NUVHD3 SiPM. We compare the amount of the predicted Cherenkov light from a gamma-induced air shower with the expected noise in the camera pixels from the NSB assuming that

<sup>7</sup>To our knowledge, this was not tested. Also possibly, a dichroic coating would increase the optical cross-talk of red photons trapped between the SiPM and the resin.

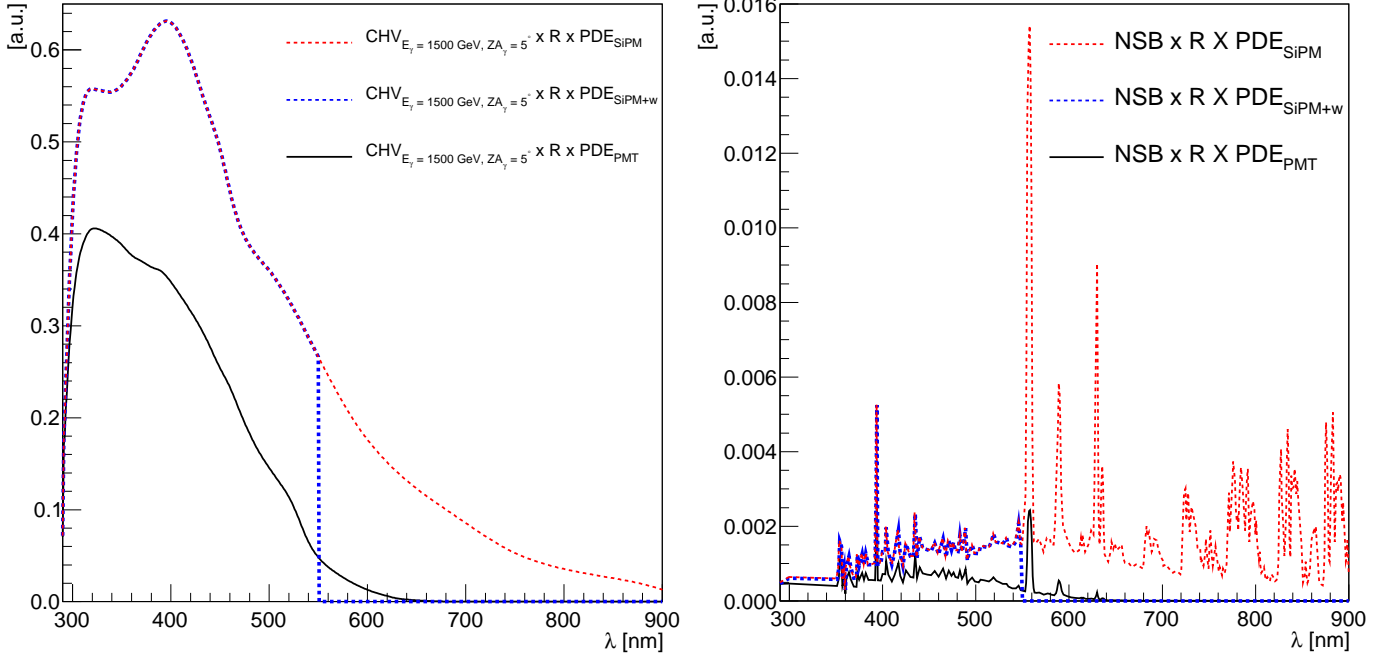


Figure 5: (left) Cherenkov photons that survive the reflection onto the reflectors of the MAGIC telescopes and are subsequently detected by a PMT (black solid line) and a SiPM (red dashed line), respectively, for a primary gamma ray of 1500 GeV and  $5^\circ$  incident angle. (right) NSB spectrum weighed with the mirror reflectivity and PDE of a PMT (black solid line) and a SiPM (red solid line), respectively. The blue dotted line is computed by artificially filtering out all wavelengths above 550 nm for reasons discussed in Sec. 4.2.

a perfect filter is used to reject photons with wavelength above  $\lambda_{\text{cut}}$ . We compute the expected SNR( $\lambda_{\text{cut}}$ ) as:

$$\text{SNR}(\lambda_{\text{cut}}) = \frac{\int_{290 \text{ nm}}^{\lambda_{\text{cut}}} \frac{dN_{\text{Ch}}}{d\lambda}(\lambda) R_{\text{mir}}(\lambda) \text{PDE}_{\text{SiPM}}(\lambda) d\lambda}{\sqrt{\int_{290 \text{ nm}}^{\lambda_{\text{cut}}} \frac{dN_{\text{NSB}}}{d\lambda} R_{\text{mir}}(\lambda) \text{PDE}_{\text{SiPM}}(\lambda) d\lambda}}, \quad (1)$$

where  $dN_{\text{Ch}}/d\lambda$  is the Cherenkov spectrum reaching the ground,  $R_{\text{mir}}(\lambda)$  is the reflectivity of the mirror,  $\text{PDE}_{\text{SiPM}}(\lambda)$  is the PDE of the SiPM and  $dN_{\text{NSB}}/d\lambda$  is the NSB spectrum observed at ground level. The background component in the denominator is taken as a square root: due to AC coupling of the photodetectors they are only sensitive to the fluctuations of the light yield rather than its absolute level. We normalise SNR( $\lambda_{\text{cut}}$ ) to the SNR( $\lambda$ ) without a filter, i.e., extending upper bound of the integral in Eq. 1 to  $\lambda = 900$  nm. The relative SNR is therefore  $\text{SNR}(\lambda_{\text{cut}})/\text{SNR}(900 \text{ nm})$  (see Fig. 6).

Fig. 6 shows that the filter improves the relative SNR if  $\lambda_{\text{cut}}$  is at around 550 nm. The improvement is of about 40% for zenith angles of  $5^\circ$ . In case the observations are performed at a larger zenith angle, the gain in the relative SNR is lower, but still of order 30%.

It is also interesting to note that the relative SNR pattern is similar also for protons of 180 GeV, which is in agreement with the results shown in Fig. 2. We display the light yield with the dichroic window as a dashed-blue line in Fig. 5. We also show in Table 2 the relative gain regarding the photon yield considering such a technical solution. We see how the NSB now still increases with respect to the PMT case but from a factor of 5.30 to a factor of 1.66 with the modified camera window, while still keeping an increase of detected Cherenkov photons

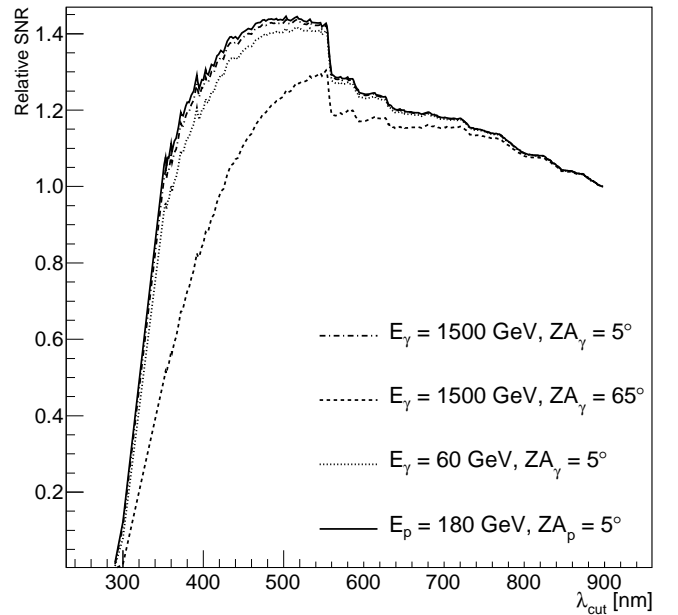


Figure 6: Expected signal-to-noise ratio (SNR) of Cherenkov and NSB light detected with a SiPM-based camera using an ideal filter cutting wavelengths above  $\lambda_{\text{cut}}$  relative to the SNR obtained without such filter. Different curves correspond to different energies and incident angles of the primary gamma ray (see legend). For comparison the relative SNR is also shown for a proton-induced EAS (solid black line).

ranging from a factor of 1.76 to 1.84 depending on the incident angle of the primary gamma ray, as reported in Table 2.

We remark that the above results cannot be directly used to estimate an increase in instrument sensitivity: the total photon yield is not a proxy for the overall instrument performance. It is now mandatory to estimate the variation in sensitivity through dedicated Monte Carlo simulations, which we do in the next section.

## 5. Simulation of a SiPM-based camera

*Simulation of SiPM.* To fully compute the sensitivity with a SiPM camera, in addition to the different PDE, we also tuned the pulse shape, the shape of the single photo-electron (phe)<sup>8</sup> distribution and trigger thresholds. The early SiPM devices suffered from very broad pulses (see e.g. [44]), the modern devices however have much narrower pulses (FWHM of 4.3 ns as reported in [22]). Even narrower 2–3 ns signals could be achieved, despite summation of signals from multiple individual SiPM devices [45]. In our simulations we assume a 3 ns FWHM of a single phe pulse. With the additional assumed spread of individual phes, the effective pulse shape is 3.5 ns.

Second, we also adjusted the response of the photodetector to a single registered phe. A PMT device has a rather broad distribution of a single phe charge. Moreover, during the multiplication of charge inside PMT, an atom might be ionized and accelerated against the flow of electrons. Such an ion hitting the photocathode produces afterpulses: large signals equivalent to even few tens of phes [46]. Due to their time delay, PMT afterpulses are not relevant for Cherenkov radiation. However, the afterpulses induced by NSB photons can mimic signals from small showers, limiting the performance of an IACT trigger. In contrast to this, the response of SiPM to light is completely different. While there are also delayed signals in SiPMs after a registered phe, they can be considered as pulses originating from not fully recovered cells. This makes their amplitudes smaller than a single phe [20], which, combined with their relatively rare occurrence, makes them negligible effect for the SiPM performance in IACT applications.

SiPMs have a single-phe resolution, i.e. the distribution of single phe amplitude is intrinsically narrow and clearly distinguishable from that of multiple phes. However, the effect of optical cross-talk introduces signal confusion. The probability of cross-talk depends on the SiPM device and its operation parameters. For example Nepomuk Otte et al. [20] obtained values of 6% – 20%. Multiple such signals can stack up, producing (with decreasing probability) multi-phe signals. This effect can affect both the Cherenkov light and NSB or dark rate induced phes. The difference of the single phe distribution for PMT and SiPM is therefore an important effect to consider. To take this into account, we produced a general single phe distribution representative of a SiPM, assuming a  $\epsilon = 15\%$  optical cross-talk. We use the formula of Gentile et al. [47], simplified to the case of a single true phe. The obtaining probability distribution of registered number  $n$  of phes is:

$$P(n) = (1 - \epsilon) \times \epsilon^{n-1}. \quad (2)$$

<sup>8</sup>For simplicity we will also refer to the signal of a single triggered SiPM cell, as a “photoelectron”, nomenclature commonly used for PMT signals.

Furthermore we assume that each phe has an intrinsic amplitude spread of 10%<sup>9</sup>. Therefore, the amplitude of a  $n$ -phe signal is drawn from a Gaussian distribution with a standard deviation equal to  $\sqrt{n} \times 10\%$  of its mean.

*Tuning of Monte Carlo simulations and analysis.* The application of modified pulse width and single phe distribution for SiPM simulations requires additional changes in how those simulations are processed with respect to PMT camera simulations. In order to integrate a similar fraction of the light pulse, in the case of SiPM we increase the size of the pulse integration window from 5 to 7 time slices. For the calibration of SiPM MC simulations we use the excess noise factor method, the same as for PMT cameras. For the simulated  $\epsilon = 15\%$  case, the excess-noise factor ( $F^2 = 1.16$ ) is comparable to the PMT one of 1.23.

When a different photosensor is considered, as the SiPM considered in this work, the higher NSB level can affect the observations in two ways: increased trigger threshold (expressed in phes) and higher noise in the images that could additionally require higher image cleaning<sup>10</sup> thresholds. An Alternate Current (AC) coupling of the MAGIC camera pixels signals is installed to prevent the mean level of the NSB to affect the observations directly. Therefore the noise effect is only related to fluctuations of the NSB, which increases only as the square root of the total increase of the NSB, see also [Sec. 4.2](#). The higher level of the NSB fluctuations might require an increase of the trigger thresholds to allow operations with a manageable rate of accidental events. However, this effect is also tangled with the difference of the single phe distribution caused by PMT afterpulses and SiPM optical cross-talk as well as with the enlarged pulse integration window. Therefore we performed a MC study to derive the expected trigger thresholds for a SiPM camera (see [Appendix A](#) for details). Using a MC study, we obtained that a SiPM camera will require a factor of about 1.7 and 1.2 higher thresholds without and with a dichroic window, respectively, to achieve the same level of accidental triggers as for the PMT camera.

The effect of the increased noise in the images is automatically taken into account, as we simulate the SiPM camera with a higher average rate of NSB phe per pixel. Nevertheless, if the noise in the images is highly increased, the image cleaning procedure might need to be revised, in particular the values of the cleaning thresholds need to be increased. We optimize the cleaning thresholds based on noise-only events (see [Appendix A.2](#) for details). Intriguingly, due to the interplay of different effects, the optimal cleaning thresholds for the case of SiPM camera without the filters turn out the same as for PMT camera. With addition of the filters the cleaning thresholds can be considerably lowered by a factor of 1.5.

It is curious that the effect on the trigger thresholds and on the cleaning thresholds during the analysis is different. We note

<sup>9</sup>The precise value of such a spread will depend on a specific hardware solution for amplification and registering the SiPM signals. We note however, that the number is expected to be small, and therefore its effect is expected to be negligible with respect to the optical cross-talk.

<sup>10</sup>The image cleaning is the reconstruction procedure in which image pixels in the camera are selected by their signal level and their geometry.

however a number of differences between those two stages. The MAGIC trigger operates on amplitudes, while the charge extraction used in further analysis exploits pulse integration. The two approaches are not equivalent when time spread of individual phes is present. Moreover, the stereoscopic trigger is based on a  $2 \times 3$ NN (next-neighbour) condition with each pixel having a signal above a given threshold. In contrast, the image cleaning in each telescope is searching for 2NN, 3NN or 4NN combinations with a sum of clipped signals above a given total threshold, applying also different time constraints than a trigger (see [48] for details). Therefore, the interplay of higher NSB rate with single phe distribution with a smaller tails can have a non trivial, and different effect on both.

To evaluate the irreducible background by cosmic rays, we simulate the response of the telescopes to proton, helium and electron induced showers. In total, we have simulated 5 M gamma rays, 25 M electrons, 125 M helium 125 M protons between  $0^\circ$  and  $35^\circ$  and 5 M gamma rays, 25 M electrons, 125 M helium 200 M protons between  $35^\circ$  and  $50^\circ$ . We normalise the cosmic-ray proton spectrum to the DAMPE measurement [49]. To take into account the effect of helium and higher elements, we apply the same approach as in [50]. Namely, we normalise the helium to  $1.6 \times 50\% = 80\%$  of the proton flux, where the 1.6 factor is the factor derived by Aleksić et al. [50] to correct for elements higher then helium. The electron simulations are weighted to the parametrised combination of the *Fermi*-LAT and H.E.S.S. all-electron spectrum applying the model of Eq. 2 from Ohishi et al. [51]. The gamma-ray simulations are normalised to the Crab Nebula spectrum following [48].

The MC simulations are analysed using the MARS software<sup>11</sup> [52, 48]. The MARS software allows to estimate the nature of the primary particle thanks to a classifier called *hadronness* which is close to 1 for hadrons and 0 for gamma-ray primaries. Further parameters computed by MARS are the estimated energy (derived by using the Random Forest method), as well as the reconstructed event direction in the sky. A proxy for this latter parameter is dubbed  $\theta^2$ , i.e. the squared angular distance between the nominal and reconstructed source direction.

## 6. Performance of MAGIC with a SiPM-based camera

*Effective area with a SiPM-based camera.* To investigate the improvement at the energy threshold of MAGIC, where the largest effect of the NSB on the event triggering and reconstruction is expected to occur, we have investigated the variation in the collection area. The results are shown in Fig. 7. At the trigger level (see the top panel), the higher PDE, despite the increase of the thresholds results in an increase of the effective area at the lowest energies. For example at 50 GeV the collection area is improved by a factor of 2 comparable to that of the PMT camera. Moreover, the reduction of noise and thus also the trigger thresholds with the use of filters allows for a further increase of the collection area at the lowest energies accessible

with MAGIC. At 50 GeV the improvement of filters is a factor  $\sim 40\%$ , resulting in a total improvement of nearly a factor of 3 with respect to the PMT camera. We also investigate the collection area at the reconstruction level, namely when both images survive the image cleaning with a minimal size. In the case of the PMT camera in the reconstruction, we applied a cut of 50 phe, commonly used in the MAGIC analysis. For the SiPM camera, we upscaled this value by 2.2 (without) or 1.7 (with filter), see Table 2. The improvement of the collection area at the reconstruction stage is comparable to the one at the trigger stage.

*Angular Resolution with a SiPM-based camera.* A preciser shower reconstruction represents a second possibility by which the improvement of the "cleaningness" of the images may possibly enhance the gamma/hadron separation. To study this, we compute the energy-dependent angular resolution for the three simulated camera cases (see Fig. 8). We apply cuts in minimal image size as done in the effective-area study. While the SiPM camera has somewhat worse angular resolution as the PMT one above 200 GeV, below 100 GeV the angular resolution is slightly improved. There is very little difference in the angular resolution with or without using filters. This shows that, except of the lowest energies, the reconstruction of the shower direction is still not strongly limited by the amount of light received by the telescopes, or the "cleaningness" of the image, but by other factors (such as geomagnetic field deflection of the shower, optical PSF of the instrument, pixelisation of the camera, ...). In fact, the increased collection area of the SiPM camera adds dim images with strong intrinsic fluctuations that are likely less precisely reconstructed, affecting slightly the overall performance.

*Sensitivity with a SiPM-based camera.* To evaluate the sensitivity, we analyse the data in bins of estimated energy. As for the previous studies of the parameters that govern the instrument performance, we apply a cut in minimal image size with a value scaled to the expected light yield for the SiPM camera. In each such bin we optimize the *hadronness* and  $\theta^2$  cuts to obtain the best differential sensitivity. We scan the values with cut efficiencies from 60% to 99% for *hadronness* and from 40% to 95% for  $\theta^2$ . The rate of gamma-ray events is computed directly for a given  $\theta^2$  cut. However, to improve the statistics for events that contribute to a diffuse background we consider events reconstructed up to  $1^\circ$  away from the camera centre, and scale the obtained rate to the much smaller background expected at the solid angle corresponding to the  $\theta^2$  value-cut. In this scaling we also correct for the drop of the efficiency with the distance from the camera centre by using a fit with a Gaussian function. The sensitivity is defined as the minimal detectable flux that satisfies three conditions: a  $5\sigma$  significance (computed according to Eq. 17 from [53] assuming three background control regions), an event excess of at least 10 events and above 5% of the residual background. To use the available statistics of background events in an optimal way, without introducing bias and overtraining the cuts, we divide the individual samples of simulated particles into  $N_s = 4$  subsamples. In the analysis of

<sup>11</sup>MARS stands for MAGIC Analysis and Reconstruction Software and is a proprietary pipeline of the MAGIC Collaboration.

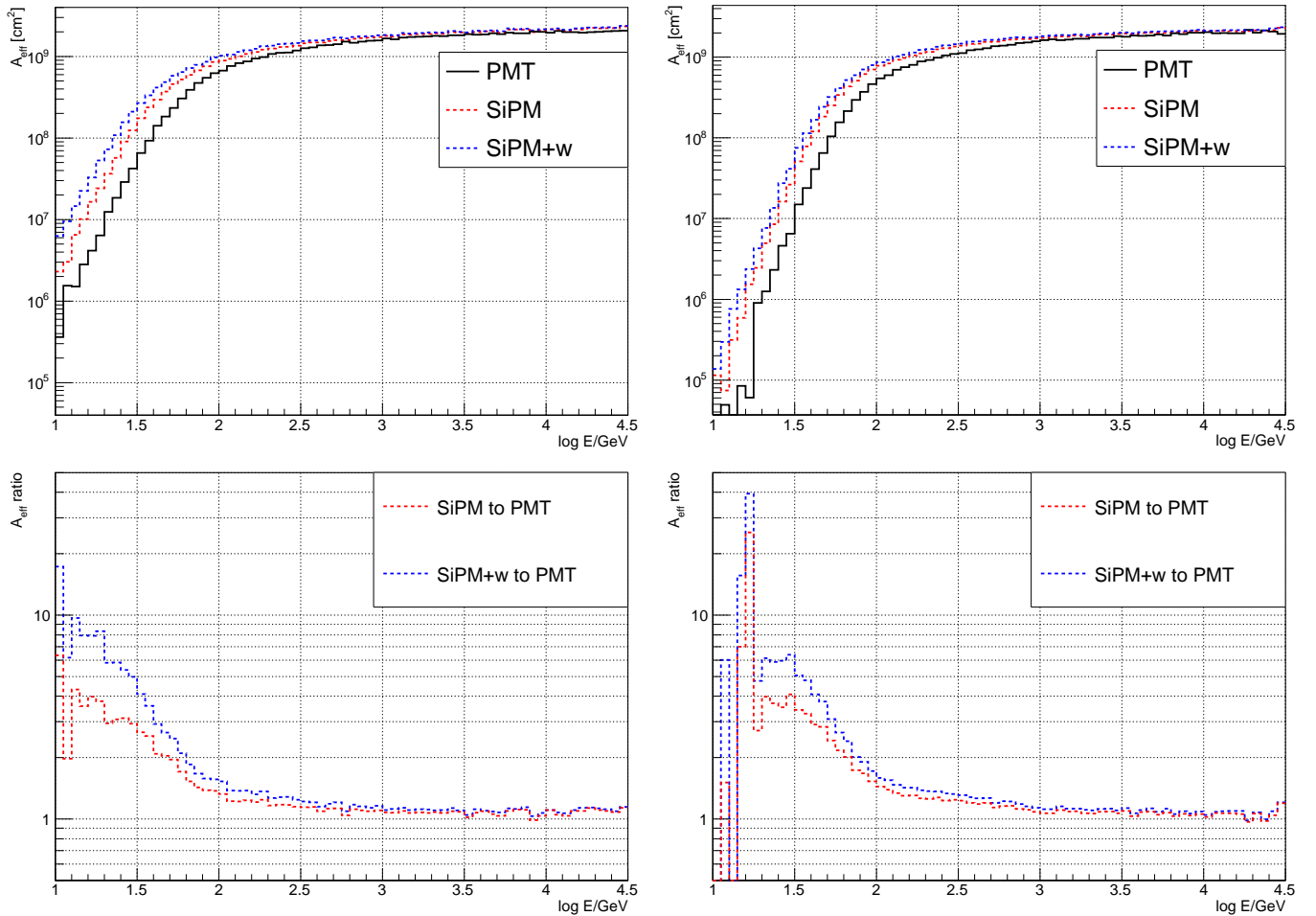


Figure 7: Averaged effective area for PMT- (black) and SiPM-based camera with (blue) and without (red) filters for low-zenith angle observations. Effective area computed at the trigger level (left panels) or at the reconstruction level (right panels). The bottom panels show the ratio of the corresponding effective area to the PMT case.

each subsample, we use  $N_s - 1$  remaining subsamples to obtain the optimal cuts, that are then applied to the original subsample. All subsamples (processed with the above-described procedure with different cuts) are then stacked together for the final result.

The expected rates for the simulated SiPM camera with and without filters are shown in Fig. 9. As expected, the residual background is dominated by protons, with an additional contribution of electrons in the energy range of a few hundred GeV. At energies below 100 GeV the ratio of the gamma-to-background rate is improved when using a SiPM camera. The combined effect of the application of filters and re-optimised cleaning thresholds does not change the rates in a qualitative way.

The obtained sensitivities are compared in Fig. 10. The improvement of the SiPM camera is clearly seen in the energy range  $\lesssim 200$  GeV for low zenith angles and  $\lesssim 1000$  GeV for medium zenith angles. For the low zenith-angle case, the improvement is a factor of three at 50 GeV (i.e., close to the threshold). At the same energy the low-pass filter in front of a SiPM camera gives an additional small boost of 20% in the sensitivity. However at higher energies the difference in sensi-

tivity by using filters is smaller, and for the energies  $\sim 1$  TeV the obtained sensitivity is actually worse. The result that a low-pass filter has rather small effect on improving the sensitivity is in line with the previous performance study regarding different light illumination levels [54] showing that moonlight which increases the NSB even by a factor of 5 has negligible ( $\lesssim 5-10\%$ ) impact on the sensitivity in most of the energy range accessible with MAGIC. In the simulated case of a SiPM camera with and without filters, the application of filters reduces the NSB level by a factor of 3.1 (see Table 2), but at the additional price of loosing 20% loss the light from the air shower.

Stronger improvement for the medium zenith observations can be caused by the shift of the observed Cherenkov spectrum towards red wavelengths caused by the atmospheric absorption. The jump in the reported SiPM camera without filters, mid-zenith sensitivity for a 5 TeV point is an artifact caused by low background statistics.

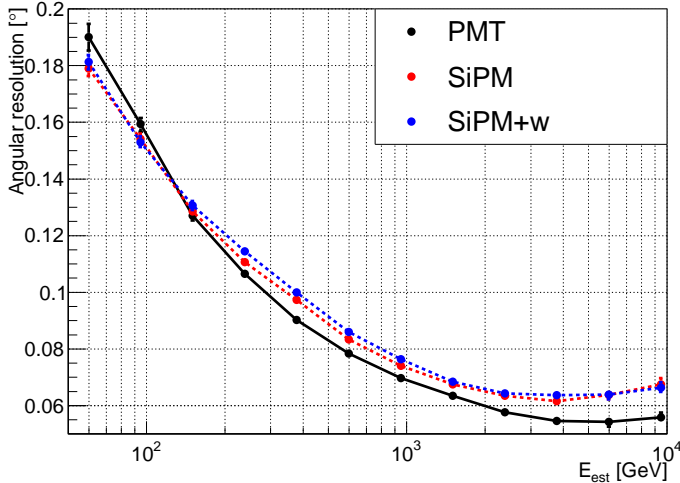


Figure 8: Angular resolution (defined as 68% containment radius) as a function of the estimated energy for the PMT (black) and the SiPM camera with (blue) and without (red) filters. Simulations at low zenith angles are used.

## 7. Discussion

In Sec. 6 we have seen how the use of SiPMs instead of PMTs may provide a sensitivity boost, which according to our generalized simulations, can amount even to about factor of three at about 50 GeV, regardless the higher sensitivity of SiPMs to the NSB. In this section we discuss the reasons for considering an upgrade of 3<sup>rd</sup> generation IACT cameras to SiPMs, as well as the problems related to the technical implementation.

About a factual implementation of a SiPM-based camera, we start by recalling that our results are not based on a full-scale design and simulation of the camera, and thus this is just a preliminary orientating work. To accurately address the performance change with a fully SiPM-based camera, one should in detail define the actual SiPM to be used, the SiPM summation electronics, at least. In the generalized SiPM simulations that we applied in this work we limited to taking care of those effects at the level expected from the available devices. Therefore we may claim our results conservatively as follows: at low energies SiPMs would provide an improved performance.

Regarding the addition of a modified plexiglass window, with dichroic properties, we also mention that, although it looks like the improvement of the performance of such a window is not very high. The biggest improvement is expected in terms of collection area, at the lowest energies, however due to simultaneous increase of background rate it does not affect sensitivity much (note that at the lowest energies the sensitivity is limited by the signal-to-background systematic condition, which means that the sensitivity scales with the background to excess rather than square root of background to excess). Such a gain in the collection area can be considered a benefit in case of some scientific targets, e.g.: observations of pulsars (where signal-to-background condition does not apply), or very short transients. Nevertheless, it seems that the additional effort, cost and complexity of installing wavelength filters is not justified performance-wise. On the other hand such filters also do not

significantly degrade the performance, thus can be considered a viable solution if the particular hardware implementation could be problematic e.g. due to pile-up of copious NSB photons. Therefore, we have contacted two companies about the technical feasibility of a dichroic window that cuts wavelengths above 550 nm. It is a substantial technological effort but we understood it is affordable. While obtaining an optimal cut (> 95% transmission below 550 nm and < 5% transmission above 550 nm) is obtained through the deposition of a series of dichroic layers, more complex is the substrate choice. The technology of shaping the light transmission through transparent materials is very advanced nowadays and achieved through repeated deposition of coating layers whose global interference pattern allows to create a dichroicity figure customizable to the percent level<sup>12</sup>. The layer deposition process is normally achievable on small surfaces at custom level or large surfaces at industrial level. Possibly arrangements in tiles can be considered, such as that used in MAGIC or VERITAS for special observation modes [55]. Glass layers, that would be the best substrate, would be too heavy and fragile, considering that the camera is subject to repentine acceleration. Plexiglass or similar materials are lighter and more flexible, however they suffer ageing from UV light, which is used in the dielectric layers deposition. Also, the deposition of homogeneous layers over a wide area is technologically a challenge, albeit possible for some companies. More easily obtained is a camera composed of few large tiles of dichroic pads held together by a thin frame.

Although we cannot support this claim without a full simulation, we are of the opinion that our results obtained for MAGIC are roughly valid also for the other two 3<sup>rd</sup> generation IACTs currently operating: H.E.S.S. and VERITAS. The boost in sensitivity at low energies would generally improve the prospects of detection for targets in which the low-energy signal is more relevant, however, it might not be sufficient to argue for a full camera upgrade for H.E.S.S. and VERITAS before the advent of CTA. However, we argue that for MAGIC it could be a viable opportunity. MAGIC was designed and constructed to be the lowest energy-threshold instrument of its kind [56]. The reason is that MAGIC has a vantage outlook to the Northern extragalactic sky, where a broadband multiwavelength coverage is facilitated. The gamma-ray signal from distant extragalactic sources suffers strong absorption in the Extragalactic Background Light fields with increasing energy if the gamma-ray, hence the need for lowest possible energy thresholds. There is a second reason why an upgrade of the camera of MAGIC could be considered. The MAGIC telescopes are located very close to where the first telescope of the Cherenkov Telescope Array North (CTA-N) is built, the LST1 telescope [57]. Additional three LST telescopes are currently under construction. LSTs are 23-m class telescopes with similar parabolic shape as the MAGIC telescopes, but with twice larger surface area that allows sampling the fainter signals of lower-energy events. Currently, LST1 is operating both as a standalone instrument and in joint observation with MAGIC, mostly because the commis-

<sup>12</sup>For a fixed incident direction.

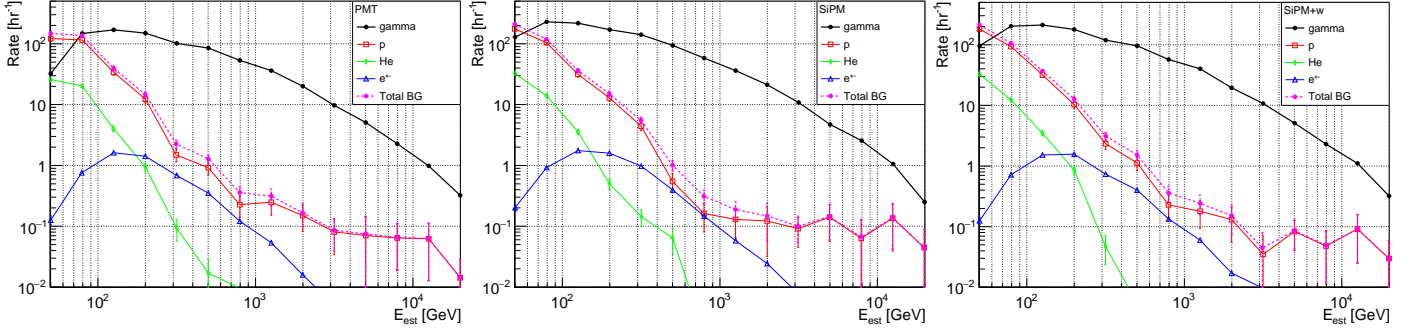


Figure 9: Simulated rates for a SiPM camera for gamma rays (black, solid line, assuming the Crab Nebula spectrum) and the residual background (protons; red squares, helium; green diamonds - including estimation of higher element contribution, all-electrons; blue triangles and total background; dashed line in magenta). The rates are computed with best-sensitivity cuts using MC simulations for low zenith angles. Left panel shows the case of the PMT camera; (middle) case of a SiPM camera without additional filters; (right) case of a SiPM camera with low-pass filter.

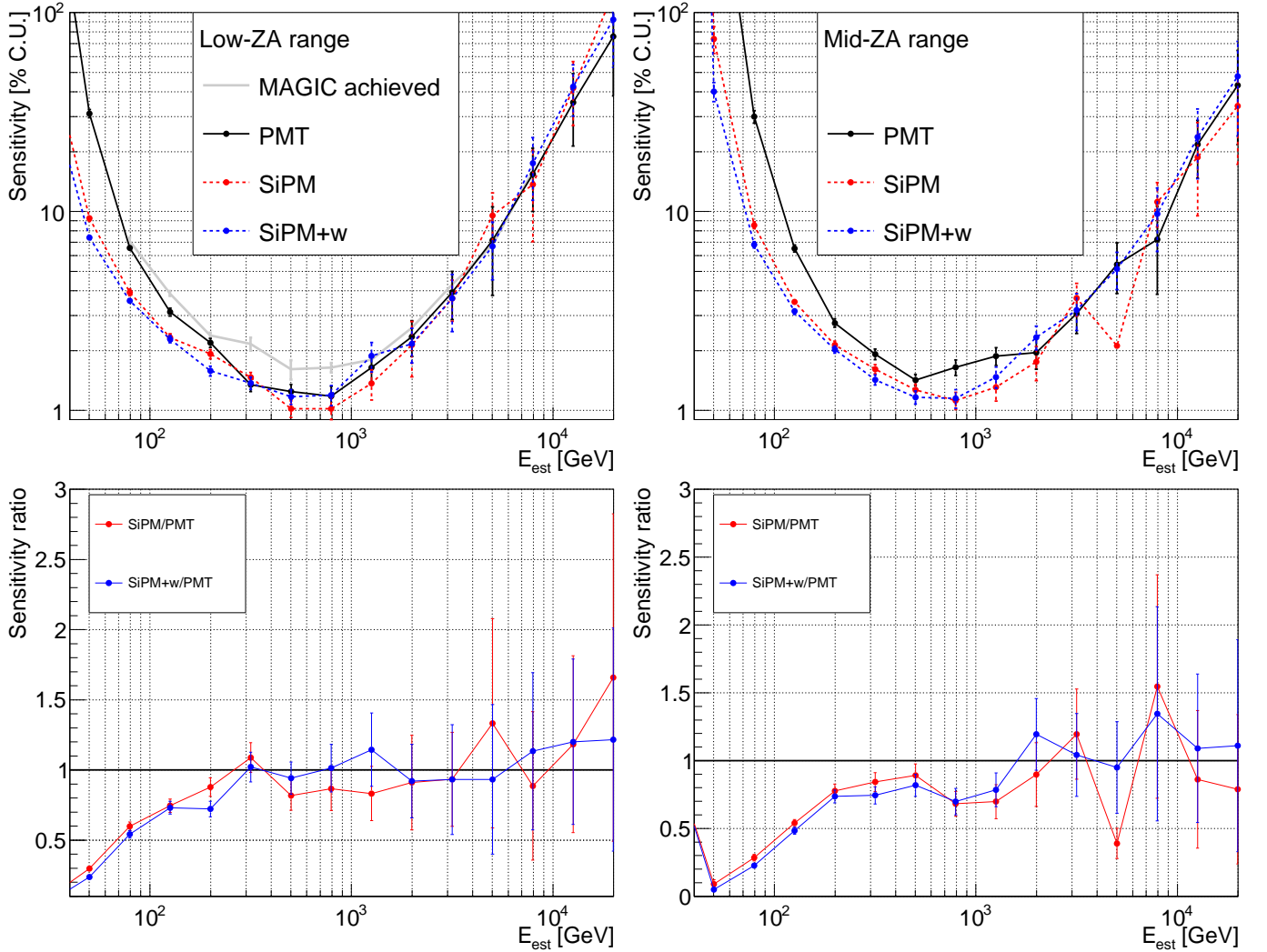


Figure 10: Sensitivity (top panels) of a SiPM camera without (red) and with low-pass filter (blue) compared with simulations of a PMT camera (black) and the achieved performance of the MAGIC telescopes (gray, [48]). (left) observations at low zenith angles ( $5 - 35^\circ$ ), (right) observations at medium zenith angles ( $35 - 50^\circ$ ). Bottom panels show the corresponding sensitivity ratios with respect to a PMT camera.

sioning of IACTs is facilitated in stereoscopic mode, because a shower location is better triangulated, but also because the joint observation allows for an improvement of about 50% in

the LST1 performance [58]. An improvement of the MAGIC sensitivity at the lowest energies would go into the direction of matching MAGIC's performance towards LST-1. We remark

however that there are no plans for the long term of MAGIC telescopes being part of the CTA-N array, so this solution could prove only temporary.

## 8. Summary and Conclusions

In this work we have discussed the possible upgrade of a current-generation IACT camera from PMTs to SiPMs (Sec. 2).

1. We have found that the spectral Cherenkov photons distribution in Table 1 and Fig. 2 at ground depends little on the energy and more on the zenith angle (except for the total yield) and this is a measurable effect when folded with the instrument spectral yield (see Sec. 4);
2. There are several factors that affect the IACT acceptance to different frequencies of the Cherenkov signal, as well as to the background and the NSB (see Sec. 3). Most of these have approximately a 'gray' (wavelength independent) response (see Fig. 4), such as the mirror reflectivity, the plexiglass window protecting the camera and the light funnels on top of the photosensors. The stronger wavelength-dependent response comes from the PDE of the photosensors. We have shown exemplary PDEs of PMTs and SiPMs showing that the typical sensitivity of SiPMs to red photons is higher w.r.t. that of PMTs (see Fig. 1)
3. We have found that by replacing PMTs with SiPMs in the camera and comparing the light yield, we have found that SiPMs would allow for a factor 2.2 to 2.5 higher signal (Table 2) regardless the energy of the primary. This strong signal boost is also accompanied by an even stronger factor of 5.3 of more light from the NSB (Fig. 5) that requires higher suppression of the NSB both at the trigger and analysis level (optimised trigger and cleaning thresholds).
4. We have investigated the performance gain through end-to-end Monte Carlo simulations and found that a SiPM-based camera would grant a factor of about three higher sensitivity at 50 GeV (for low zenith-angle observations), with decreasing improvement for higher energies (Fig. 10). This is due to the fact that the higher-energy showers are optimally reconstructed even with a less sensitive photosensor. At medium zenith angles some improvement is seen up to 1 TeV energies.
5. We have investigated the possibility of reducing the sensitivity to the red part of the spectrum, specially intense in the NSB. We have found that by replacing the plexiglass with a dichroic window, we could still gain a factor  $\sim 1.8$  more signal from the showers and only a factor of 1.7 more light from the NSB. However, this solution only moderately improves the sensitivity with respect to a neutral plexiglass in combination with a SiPM camera (Fig. 10). This is because the sensitivity of MAGIC is only affected at very high NSB level.
6. The simulations show that a SiPM camera will also display slightly better at low energies, angular resolution (Fig. 8), however at higher energies the effect is inverted.

7. Additionally (especially if equipped with filters) the SiPM camera will provide a better effective area at low energies (Fig. 7).
8. We have discussed the technical implementation of such cameras in Sec. 7, finding that our estimates could be quite accurate or, in worst case, conservative.

Replacing the PMTs of the MAGIC cameras with SiPMs would be a costly intervention, but it could be a valid investment for MAGIC in prolonging its scientific competitiveness and in connection to CTA.

*Acknowledgments.* The authors warmly thank the anonymous referees who carefully checked the first version of the manuscript and suggested further checks will lead to improvement of our results. The authors would also like to thank the MAGIC Collaboration for allowing to use their simulation and analysis tools for performing this study. We especially acknowledge A. Hanh for useful comments on the manuscript. and D. De Paoli, R. Rando and M. Mariotti for useful discussions. MD acknowledges funding from Italian Ministry of Education, University and Research (MIUR) through the "Dipartimenti di eccellenza" project Science of the Universe. JS is supported by Narodowe Centrum Nauki grant number 2019/34/E/ST9/00224.

## References

- [1] A. M. Hillas. Evolution of ground-based gamma-ray astronomy from the early days to the Cherenkov Telescope Arrays. *Astropart. Phys.*, 43:19–43, 2013. doi: 10.1016/j.astropartphys.2012.06.002.
- [2] E. Lorenz, Robert Wagner, and R. Wagner. Very-high energy gamma-ray astronomy: A 23-year success story in high-energy astroparticle physics. *Eur. Phys. J.*, H37:459–513, 2012. doi: 10.1140/epjh/e2012-30016-x.
- [3] M. L. Ahnen et al. Performance of the MAGIC telescopes under moonlight. *Astropart. Phys.*, 94:29–41, 2017. doi: 10.1016/j.astropartphys.2017.08.001.
- [4] Sean Griffin. VERITAS Observations under Bright Moonlight. *PoS, ICRC2015:989*, 2016. doi: 10.22323/1.236.0989.
- [5] M. Doro et al. The reflective surface of the MAGIC telescope. *Nucl. Instrum. Meth.*, A595:200–203, 2008. doi: 10.1016/j.nima.2008.07.073.
- [6] R. Winston. Light collection within the framework of geometrical optics. *Journal of the Optical Society of America*, 2:245, 1970.
- [7] R. Winston and W. Welford. *High Collection for Nonimaging Optics*. Academic Press, 1989.
- [8] A. Hahn, A. Dettlaff, D. Fink, D. Mazin, R. Mirzoyan, and M. Teshima. Development of three silicon photomultiplier detector modules for the MAGIC telescopes for a performance comparison to PMTs. *Nuclear Instruments and Methods in Physics Research A*, 912:259–263, December 2018. doi: 10.1016/j.nima.2017.11.071.
- [9] Michele Doro. CTA - A Project for a New Generation of Cherenkov Telescopes. *Nucl. Instrum. Meth.*, A630:285–290, 2011. doi: 10.1016/j.nima.2010.06.085.
- [10] M. Actis et al. Design concepts for the Cherenkov Telescope Array CTA: An advanced facility for ground-based high-energy gamma-ray astronomy. *Exper. Astron.*, 32:193–316, 2011. doi: 10.1007/s10686-011-9247-0.
- [11] B. S. Acharya et al. "introducing the cta concept". *Astropart. Phys.*, 43, 2013.
- [12] Matthieu Heller et al. An innovative silicon photomultiplier digitizing camera for gamma-ray astronomy. *Eur. Phys. J.*, C77(1):47, 2017. doi: 10.1140/epjc/s10052-017-4609-z.
- [13] Riccardo Rando et al. Silicon Photomultiplier Research and Development Studies for the Large Size Telescope of the Cherenkov Telescope Array. *PoS, ICRC2015:940*, 2016. doi: 10.22323/1.236.0940.

- [14] C. Arcaro, D. Corti, A. De Angelis, M. Doro, C. Manea, M. Mariotti, R. Rando, I. Reichardt, and D. Tesaro. Studies on a silicon-photomultiplier-based camera for Imaging Atmospheric Cherenkov Telescopes. *Nucl. Instrum. Meth.*, A876:26–30, 2017. doi: 10.1016/j.nima.2016.12.055.
- [15] M. Mallamaci et al. Design of a SiPM-based cluster for the Large-Sized Telescope camera of the Cherenkov Telescope Array. *Nucl. Instrum. Meth.*, A936:231–232, 2019. doi: 10.1016/j.nima.2018.09.141.
- [16] C. Perennes, M. Doro, et al. Optical feasibility of an upgrade of the CTA LST camera to SiPM. *Proceedings of*, 2020.
- [17] Stefan Gundacker and Arjan Heering. The silicon photomultiplier: fundamentals and applications of a modern solid-state photon detector. *Physics in Medicine & Biology*, 65(17):17TR01, aug 2020. doi: 10.1088/1361-6560/ab7b2d. URL <https://doi.org/10.1088/1361-6560/ab7b2d>.
- [18] D. Nakajima, D. Fink, J. Hose, R. Mirzoyan, D. Paneque, K. Saito, T. Schweizer, M. Teshima, T. Toyama, and H. Wetteskind. New Imaging Camera for the MAGIC-I Telescope. In *International Cosmic Ray Conference*, volume 33 of *International Cosmic Ray Conference*, page 3044, January 2013.
- [19] A. Gola, F. Acerbi, Capasso, M., et al. Nuv-sensitive silicon photomultiplier technologies developed at fondazione bruno kessler. *Sensors (Basel, Switzerland)*, 19(2):308, Jan 2019. doi: doi:10.3390/s19020308.
- [20] Adam Nepomuk Otte, Distefano Garcia, Thanh Nguyen, and Dhruv Purushotham. Characterization of Three High Efficiency and Blue Sensitive Silicon Photomultipliers. *Nucl. Instrum. Meth. A*, 846:106–125, 2017. doi: 10.1016/j.nima.2016.09.053.
- [21] D. Nakajima. Private communication, 2019.
- [22] D. Depaoli, A. Chiavassa, D. Corti, F. Di Pierro, M. Mariotti, and R. Rando. Development of a SiPM Pixel prototype for the Large-Sized Telescope of the Cherenkov Telescope Array. *Nucl. Instrum. Meth. A*, 1055:168521, 2023. doi: 10.1016/j.nima.2023.168521.
- [23] Colin B. Adams et al. Design and performance of the prototype Schwarzschild-Couder telescope camera. *J. Astron. Telesc. Instrum. Syst.*, 8(1):014007, 2022. doi: 10.1117/1.JATIS.8.1.014007.
- [24] Ivan Rech, Antonino Ingargiola, Roberto Spinelli, Ivan Labanca, Stefano Marangoni, Massimo Ghioni, and Sergio Cova. Optical crosstalk in single photon avalanche diode arrays: a new complete model. *Opt. Express*, 16(12):8381–8394, Jun 2008. doi: 10.1364/OE.16.008381. URL <https://opg.optica.org/oe/abstract.cfm?URI=oe-16-12-8381>.
- [25] F. Rehbein et al. Calibration of 122 SensL MicroFJ-60035 SiPMs and the reduction of optical crosstalk due to coupled light guides. *Accepted for publication in Revista Mexicana de Astronomia y Astrofisica*, 2023.
- [26] B. Huber, I. Braun, and H. Anderhub. Solid light concentrators for small-sized photosensors used in Cherenkov telescopes. In *32nd International Cosmic Ray Conference*, volume 9, page 2, 2011. doi: 10.7529/ICRC2011/V09/0136.
- [27] J. A. Aguilar, A. Basili, V. Boccone, F. Cadoux, A. Christov, D. della Volpe, T. Montaruli, E. Platos, and M. Rameez. Design, optimization and characterization of the light concentrators of the single-mirror small size telescopes of the Cherenkov Telescope Array. *Astropart. Phys.*, 60:32–40, 2015. doi: 10.1016/j.astropartphys.2014.05.010.
- [28] Alexander Hahn, Antonios Dettlaff, David Fink, Daniel Mazin, Razmik Mirzoyan, and Masahiro Teshima. Results of the Parallel Operation of Large-Size SiPM Detector Modules and PMTs in IACTs. *JPS Conf. Proc.*, 27:011010, 2019. doi: 10.7566/JSPSCP.27.011010.
- [29] A. Biland et al. Calibration and performance of the photon sensor response of FACT – The First G-APD Cherenkov telescope. *JINST*, 9(10):P10012, 2014. doi: 10.1088/1748-0221/9/10/P10012.
- [30] Max Ludwig Knoetig et al. FACT - Long-term stability and observations during strong Moon light. In *33rd International Cosmic Ray Conference*, page 0695, 7 2013.
- [31] Daniela Dorner et al. FACT - Highlights from more than Eight Years of Unbiased TeV Monitoring. *PoS, ICRC2021:851*, 2021. doi: 10.22323/1.395.0851.
- [32] D. Heck, J. Knapp, J. N. Capdevielle, G. Schatz, and T. Thouw. CORSIKA: A Monte Carlo code to simulate extensive air showers. 2 1998.
- [33] M. Haffke. *Berechnung und Implementierung neuer Atmosphärenmodelle in die MAGIC MonteCarlo Kette*. PhD thesis, University of Dortmund, 2007.
- [34] B. Rossi and K. Greisen. Cosmic-ray theory. *Rev. Mod. Phys.*, 13, 1941.
- [35] Christian Fruck, Markus Gaug, Alexander Hahn, Victor Acciari, Jürgen Besenrieder, Dijana Dominis Prester, Daniela Dorner, David Fink, Lluís Font, Saša Mićanović, Razmik Mirzoyan, Dominik Müller, Lovro Pavletić, Felix Schmuckermaier, and Martin Will. Characterizing the aerosol atmosphere above the Observatorio del Roque de los Muchachos by analysing seven years of data taken with an GaAsP HPD-readout, absolutely calibrated elastic LIDAR. *MNRAS*, 515(3):4520–4550, September 2022. doi: 10.1093/mnras/stac1563.
- [36] V. A. Acciari et al. MAGIC very large zenith angle observations of the Crab Nebula up to 100 TeV. *Astron. Astrophys.*, 635:A158, 2020. doi: 10.1051/0004-6361/201936899.
- [37] C. R. Benn and S. L. Ellison. Brightness of the night sky over la palma. *New Astronomy Reviews*, 42:503, 1998.
- [38] Michele Doro. *Novel Reflective Elements and Indirect Dark Matter Searches for MAGIC II and Future IACTs*. PhD thesis, Padua U., 2009. URL <https://magicold.mpp.mpg.de/publications/theses/MDoro.pdf>.
- [39] M. Will, R. Mirzoyan, J. van Scherpenberg, and M. Garzarczyk. Novel Back-coated Glass Mirrors for the MAGIC Telescopes. In *36th International Cosmic Ray Conference (ICRC2019)*, volume 36 of *International Cosmic Ray Conference*, page 823, July 2019. doi: 10.22323/1.358.0823.
- [40] D. Bastieri et al. Development and production of light-weight all-aluminium mirrors for the MAGIC telescope. In *7th Workshop on Towards a Network of Atmospheric Cherenkov Detectors 2005*, pages 593–597, 4 2005.
- [41] F. Hénault et al. Design of light concentrators for cherenkov telescope observatories. In *Proc. SPIE Int. Soc. Opt. Eng.*, 2013.
- [42] A. Okumura and T.V. Dang and S. Ono and S. Tanaka and M. Hayashida and J. Hinton and H. Katagiri and K. Noda and M. Teshima and T. Yamamoto and T. Yoshida. Prototyping Hexagonal Light Concentrators Using High-Reflectance Specular Films for the Large-Sized Telescopes of the Cherenkov Telescope Array. *JINST*, 12:P12008, 2017. doi: 10.1088/1748-0221/12/12/P12008.
- [43] Andreas Förster et al. Mirror Development for the Cherenkov Telescope Array. In *33rd International Cosmic Ray Conference*, page 0747, 7 2013.
- [44] José Manuel Yebras, Pedro Antoranz, and José Miguel Miranda. Strategies for shortening the output pulse of silicon photomultipliers. *Optical Engineering*, 51(7):074004-074004-8, July 2012. doi: 10.1117/1.OE.51.7.074004.
- [45] G. Ambrosi, D. Corti, M. Ionica, C. Manea, M. Mariotti, R. Rando, I. Reichardt, and C. Schultz. Large size SiPM matrix for Imaging Atmospheric Cherenkov Telescopes applications. *Nucl. Instrum. Meth. A*, 824:125–127, 2016. doi: 10.1016/j.nima.2016.01.062.
- [46] Nural Akchurin and Heejong Kim. A study on ion initiated photomultiplier afterpulses. *Nuclear Instruments and Methods in Physics Research A*, 574(1):121–126, April 2007. doi: 10.1016/j.nima.2007.01.093.
- [47] Simonetta Gentile, Ekaterina Kuznetsova, and Franco Meddi. Photon detection efficiency of Geiger-mode avalanche photodiodes. *arXiv e-prints*, art. arXiv:1006.3263, June 2010. doi: 10.48550/arXiv.1006.3263.
- [48] J. Aleksić, S. Ansoldi, L. A. Antonelli, P. Antoranz, A. Babic, P. Bangale, M. Barceló, J. A. Barrio, J. Becerra González, W. Bednarek, E. Bernardini, B. Biasuzzi, A. Biland, M. Bitossi, O. Blanch, S. Bonney, G. Bonnoli, F. Borracci, T. Bretz, E. Carmona, A. Carosi, R. Cecchi, P. Colin, E. Colombo, J. L. Contreras, D. Corti, J. Cortina, S. Covino, P. Da Vela, F. Dazzi, A. De Angelis, G. De Caneva, B. De Lotto, E. de Oña Wilhelmi, C. Delgado Mendez, A. Dettlaff, D. Dominis Prester, D. Dorner, M. Doro, S. Einecke, D. Eisenacher, D. Elsaesser, D. Fidalgo, D. Fink, M. V. Fonseca, L. Font, K. Frantzen, C. Fruck, D. Galindo, R. J. García López, M. Garzarczyk, D. Garrido Terrats, M. Gaug, G. Giavitto, N. Godinović, A. González Muñoz, S. R. Gozzini, W. Haberler, D. Hadasch, Y. Hanabata, M. Hayashida, J. Herrera, D. Hildebrand, J. Hose, D. Hrupec, W. Idec, J. M. Illa, V. Kadenius, H. Kellermann, M. L. Knoetig, K. Kodani, Y. Konno, J. Krause, H. Kubo, J. Kushida, A. La Barbera, D. Lelas, J. L. Lemus, N. Lewandowska, E. Lindfors, S. Lombardi, F. Longo, M. López, R. López-Coto, A. López-Oramas, A. Lorca, E. Lorenz, I. Lozano, M. Makariev, K. Mallot, G. Maneva, N. Mankuzhiyil, K. Mannheim, L. Maraschi, B. Marcote, M. Mariotti, M. Martínez, D. Mazin, U. Menzel, J. M. Miranda, R. Mirzoyan, A. Moralejo, P. Munar-Adrover, D. Nakajima, M. Negrello, V. Neustroev, A. Niedzwiecki, K. Nilsson, K. Nishijima, K. Noda, R. Orito, A. Overkemping, S. Paiano, M. Palatiello,

- D. Paneque, R. Paoletti, J. M. Paredes, X. Paredes-Fortuny, M. Persic, J. Poutanen, P. G. Prada Moroni, E. Prandini, I. Puljak, R. Reinthal, W. Rhode, M. Ribó, J. Rico, J. Rodriguez Garcia, S. Rügamer, T. Saito, K. Saito, K. Satalecka, V. Scalzotto, V. Scapin, C. Schultz, J. Schlammer, S. Schmidl, T. Schweizer, S. N. Shore, A. Sillanpää, J. Sitarek, I. Snidaric, D. Sobczynska, F. Spanier, A. Stamerra, T. Steinbring, J. Storz, M. Strzys, L. Takalo, H. Takami, F. Tavecchio, L. A. Tejedor, P. Temnikov, T. Terzić, D. Tescaro, M. Teshima, J. Thaele, O. Tibolla, D. F. Torres, T. Toyama, A. Treves, P. Vogler, H. Wettskind, M. Will, and R. Zanin. The major upgrade of the MAGIC telescopes, Part II: A performance study using observations of the Crab Nebula. *Astroparticle Physics*, 72:76–94, January 2016. doi: 10.1016/j.astropartphys.2015.02.005.
- [49] Q. An, R. Asfandiyarov, P. Azzarelli, P. Bernardini, X. J. Bi, M. S. Cai, J. Chang, D. Y. Chen, H. F. Chen, J. L. Chen, W. Chen, M. Y. Cui, T. S. Cui, H. T. Dai, A. D’Amone, A. De Benedittis, I. De Mitri, M. Di Santo, M. Ding, T. K. Dong, Y. F. Dong, Z. X. Dong, G. Donvito, D. Droz, J. L. Duan, K. K. Duan, D. D’Urso, R. R. Fan, Y. Z. Fan, F. Fang, C. Q. Feng, L. Feng, P. Fusco, V. Gallo, F. J. Gan, M. Gao, F. Gargano, K. Gong, Y. Z. Gong, D. Y. Guo, J. H. Guo, X. L. Guo, S. X. Han, Y. M. Hu, G. S. Huang, X. Y. Huang, Y. Y. Huang, M. Ionica, W. Jiang, X. Jin, J. Kong, S. J. Lei, S. Li, W. L. Li, X. Li, X. Q. Li, Y. Li, Y. F. Liang, Y. M. Liang, N. H. Liao, C. M. Liu, H. Liu, J. Liu, S. B. Liu, W. Q. Liu, Y. Liu, F. Loparco, C. N. Luo, M. Ma, P. X. Ma, S. Y. Ma, T. Ma, X. Y. Ma, G. Marsella, M. N. Mazziotta, D. Mo, X. Y. Niu, X. Pan, W. X. Peng, X. Y. Peng, R. Qiao, J. N. Rao, M. M. Salinas, G. Z. Shang, W. H. Shen, Z. Q. Shen, Z. T. Shen, J. X. Song, H. Su, M. Su, Z. Y. Sun, A. Surdo, X. J. Teng, A. Tykhonov, S. Vitillo, C. Wang, H. Wang, H. Y. Wang, J. Z. Wang, L. G. Wang, Q. Wang, S. Wang, X. H. Wang, X. L. Wang, Y. F. Wang, Y. P. Wang, Y. Z. Wang, Z. M. Wang, D. M. Wei, J. J. Wei, Y. F. Wei, S. C. Wen, D. Wu, J. Wu, L. B. Wu, S. S. Wu, X. Wu, K. Xi, Z. Q. Xia, H. T. Xu, Z. H. Xu, Z. L. Xu, Z. Z. Xu, G. F. Xue, H. B. Yang, P. Yang, Y. Q. Yang, Z. L. Yang, H. J. Yao, Y. H. Yu, Q. Yuan, C. Yue, J. J. Zang, F. Zhang, J. Y. Zhang, J. Z. Zhang, P. F. Zhang, S. X. Zhang, W. Z. Zhang, Y. Zhang, Y. J. Zhang, Y. L. Zhang, Y. P. Zhang, Y. Q. Zhang, Z. Zhang, Z. Y. Zhang, H. Zhao, H. Y. Zhao, X. F. Zhao, C. Y. Zhou, Y. Zhou, X. Zhu, Y. Zhu, and S. (DAMPE Collaboration) Zimmer. Measurement of the cosmic ray proton spectrum from 40 gev to 100 tev with the dampe satellite. *Science Advances*, 5(9), 2019. doi: 10.1126/sciadv.aax3793. URL <https://advances.sciencemag.org/content/5/9/eaax3793>.
- [50] J. Aleksić, E. A. Alvarez, L. A. Antonelli, P. Antoranz, M. Asensio, M. Backes, J. A. Barrio, D. Bastieri, J. Becerra González, W. Bednarek, A. Berdyugin, K. Berger, E. Bernardini, A. Biland, O. Blanch, R. K. Bock, A. Boller, G. Bonnoli, D. Borla Tridon, I. Braun, T. Bretz, A. Cañellas, E. Carmona, A. Carosi, P. Colin, E. Colombo, J. L. Contreras, J. Cortina, L. Cossio, S. Covino, F. Dazzi, A. de Angelis, G. de Caneva, E. de Cea Del Pozo, B. de Lotto, C. Delgado Mendez, A. Domingo Ortega, M. Doert, A. Domínguez, D. Dominis Prester, D. Dorner, M. Doro, D. Elsaesser, D. Ferenc, M. V. Fonseca, L. Font, C. Fruck, R. J. García López, M. Garczarczyk, D. Garrido, G. Giavitto, N. Godinović, D. Hadasch, D. Häfner, A. Herrero, D. Hildebrand, D. Höhne-Mönch, J. Hose, D. Hrupec, B. Huber, T. Jogle, H. Kellermann, S. Klepser, T. Krähenbühl, J. Krause, A. La Barbera, D. Lelas, E. Leonardo, E. Lindfors, S. Lombardi, M. López, A. López-Oramas, E. Lorenz, M. Makariev, G. Maneva, N. Mankuzhiyil, K. Mannheim, L. Maraschi, M. Mariotti, M. Martínez, D. Mazin, M. Meucci, J. M. Miranda, R. Mirzoyan, H. Miyamoto, J. Moldón, A. Moralejo, P. Munar-Adrover, D. Nieto, K. Nilsson, R. Orito, I. Oya, D. Paneque, R. Paoletti, S. Pardo, J. M. Paredes, S. Partini, M. Pasanen, F. Pauss, M. A. Perez-Torres, M. Persic, L. Peruzzo, M. Pilia, J. Pochon, F. Prada, P. G. Prada Moroni, E. Prandini, I. Puljak, I. Reichardt, R. Reinthal, W. Rhode, M. Ribó, J. Rico, S. Rügamer, A. Saggion, K. Saito, T. Y. Saito, M. Salvati, K. Satalecka, V. Scalzotto, V. Scapin, C. Schultz, T. Schweizer, M. Shayduk, S. N. Shore, A. Sillanpää, J. Sitarek, I. Snidaric, D. Sobczynska, F. Spanier, S. Spiro, V. Stamatescu, A. Stamerra, B. Steinke, J. Storz, N. Strah, T. Surić, L. Takalo, H. Takami, F. Tavecchio, P. Temnikov, T. Terzić, D. Tescaro, M. Teshima, O. Tibolla, D. F. Torres, A. Treves, M. Uellenbeck, H. Vankov, P. Vogler, R. M. Wagner, Q. Weitzel, V. Zabalza, F. Zandanel, and R. Zanin. Performance of the MAGIC stereo system obtained with Crab Nebula data. *Astroparticle Physics*, 35(7):435–448, February 2012. doi: 10.1016/j.astropartphys.2011.11.007.
- [51] Michiko Ohishi, Luan Arbeletche, Vitor de Souza, Gernot Maier, Konrad Bernlöhner, Abelardo Moralejo Olaizola, Johan Bregeon, Luisa Arrabito, and Takanori Yoshikoshi. Effect of the uncertainty in the hadronic interaction models on the estimation of the sensitivity of the Cherenkov Telescope Array. *arXiv e-prints*, art. arXiv:2105.05822, May 2021.
- [52] Roberta Zanin, Emiliano Carmona, Julian Sitarek, Pierre Colin, Katharina Frantzen, Markus Gaug, Saverio Lombardi, Marcos Lopez, Abelardo Moralejo, Konstancja Satalecka, Valeria Scapin, and Victor Stamatescu. MARS, The MAGIC Analysis and Reconstruction Software. In *International Cosmic Ray Conference*, volume 33 of *International Cosmic Ray Conference*, page 2937, January 2013.
- [53] T. P. Li and Y. Q. Ma. Analysis methods for results in gamma-ray astronomy. *ApJ*, 272:317–324, September 1983. doi: 10.1086/161295.
- [54] M. L. Ahnen et al. Performance of the MAGIC telescopes under moonlight. *Astropart. Phys.*, 94:29–41, 2017. doi: 10.1016/j.astropartphys.2017.08.001.
- [55] Daniel Guberman, J. Cortina, R. García, J. Herrera, M. Manganaro, A. Moralejo, J. Rico, and M. Will. Using UV-pass filters for bright Moon observations with MAGIC. *PoS, ICRC2015:1237*, 2016. doi: 10.22323/1.236.1237.
- [56] Michele Doro. Reaching the lowest energy threshold of ground-based Cherenkov telescopes with MAGIC-stereo: A goal achieved. *Nucl. Instrum. Meth. A*, 692:201–207, 2012. doi: 10.1016/j.nima.2011.12.115.
- [57] CTA-LST Project, :, H. Abe, K. Abe, S. Abe, A. Aguasca-Cabot, I. Agudo, N. Alvarez Crespo, L. A. Antonelli, C. Aramo, A. Arbet-Engels, C. Arcaro, M. Artero, K. Asano, P. Aubert, A. Baktash, A. Bamba, A. Baquero Larriva, L. Baroncelli, U. Barres de Almeida, J. A. Barrio, I. Batkovic, J. Baxter, J. Becerra González, E. Bernardini, M. I. Bernardos, J. Bernete Medrano, A. Berti, P. Bhattacharjee, N. Biederbeck, C. Bigongiari, E. Bissaldi, O. Blanch, G. Bonnoli, P. Bordas, A. Borghese, A. Bulgarelli, I. Burelli, M. Buscemi, M. Cardillo, S. Caroff, A. Carosi, F. Cassol, D. Cauz, G. Ceribella, Y. Chai, K. Cheng, A. Chiavassa, M. Chikawa, L. Chytka, A. Cifuentes, J. L. Contreras, J. Cortina, H. Costantini, G. D’Amico, M. Dalchenko, A. De Angelis, M. de Bony de Lavergne, B. De Lotto, R. de Menezes, G. Deleglise, C. Delgado, J. Delgado Mengual, D. della Volpe, M. Dellaiera, D. Depaoli, A. Di Piano, F. Di Pierro, R. Di Tria, L. Di Venere, C. Díaz, R. M. Dominik, D. Dominis Prester, A. Donini, D. Dorner, M. Doro, D. Elsässer, G. Emery, J. Escudero, V. Fallah Ramazani, G. Ferrara, F. Ferrarotto, A. Fiasson, L. Freixas Coromina, S. Fröse, S. Fukami, Y. Fukazawa, E. Garcia, R. Garcia López, C. Gasbarra, D. Gasparrini, F. Geyer, J. Giesbrecht Paiva, N. Giglietto, F. Giordano, E. Giro, P. Gliwny, N. Godinovic, R. Grau, D. Green, J. Green, S. Gunji, J. Hackfeld, D. Hadasch, A. Hahn, K. Hashiyama, T. Hassan, K. Hayashi, L. Heckmann, M. Heller, J. Herrera Llorente, K. Hirotani, D. Hoffmann, D. Horns, J. Houles, M. Hrabovsky, D. Hrupec, D. Hui, M. Hütten, M. Iarlori, R. Imazawa, T. Inada, Y. Inome, K. Ioka, M. Iori, K. Ishio, Y. Iwamura, M. Jacquemont, I. Jimenez Martinez, J. Jurysek, M. Kagaya, V. Karas, H. Katagiri, J. Kataoka, D. Kerszberg, Y. Kobayashi, A. Kong, H. Kubo, J. Kushida, M. Lainez, G. Lamanna, A. Lamas-tra, T. Le Flour, M. Linhoff, F. Longo, R. López-Coto, M. López-Moya, A. López-Oramas, S. Loporchio, A. Lorini, P. L. Luque-Escamilla, P. Majumdar, M. Makariev, D. Mandat, M. Manganaro, G. Manicò, K. Mannheim, M. Mariotti, P. Marquez, G. Marsella, J. Martí, O. Martinez, G. Martínez, M. Martínez, P. Marusevec, A. Mas-Aguilar, G. Maurin, D. Mazin, E. Mestre Guillen, S. Micanovic, D. Miceli, T. Miener, J. M. Miranda, R. Mirzoyan, T. Mizuno, M. Molero Gonzalez, E. Molina, T. Montaruli, I. Monteiro, A. Moralejo, D. Morcuende, A. Morselli, K. Mrakovcic, K. Murase, A. Nagai, S. Nagataki, T. Nakamori, L. Nickel, M. Nieves, K. Nishijima, K. Noda, D. Nosek, S. Nozaki, M. Ohishi, Y. Ohtani, T. Oka, N. Okazaki, A. Okumura, R. Orito, J. Otero-Santos, M. Palatiello, D. Paneque, F. R. Pantaleo, R. Paoletti, J. M. Paredes, M. Pech, M. Pecimotika, M. Peresano, A. Pérez, E. Pietropaolo, G. Pirola, C. Plard, F. Podobnik, V. Poireau, M. Polo, E. Pons, E. Prandini, J. Prast, G. Principe, C. Priyadarshi, M. Prouza, R. Rando, W. Rhode, M. Ribó, V. Rizi, G. Rodriguez Fernandez, J. E. Ruiz, T. Saito, S. Sakurai, D. A. Sanchez, T. Šarić, Y. Sato, F. G. Saturni, B. Schleicher, F. Schmuckermaier, J. L. Schubert, F. Schussler, T. Schweizer, M. Seglar Arroyo, R. Silvia, J. Sitarek, V. Sliusar, A. Spolon, J. Strišković, M. Strzys, Y. Suda, Y. Sunada, H. Tajima, H. Takahashi, M. Takahashi, J. Takata, R. Takeishi, P. H. T. Tam, S. J. Tanaka, D. Tateishi, L. A. Tejedor, P. Temnikov, Y. Terada, K. Terauchi, T. Terzic, M. Teshima, M. Tluczykont,

F. Tokanai, D. F. Torres, P. Travnicek, S. Truzzi, A. Tutone, G. Uhlrich, M. Vacula, P. Vallania, J. van Scherpenberg, M. Vázquez Acosta, V. Verguilo, I. Viale, A. Vigliano, C. F. Vigorito, V. Vitale, G. Voutsinas, I. Vovk, T. Vuillaume, R. Walter, M. Will, T. Yamamoto, R. Yamazaki, T. Yoshida, T. Yoshikoshi, N. Zywuca, K. Bernloehr, O. Gueta, K. Kosack, G. Maier, J. Watson, University of Rijeka, Department of Physics, Rijeka, Croatia, Institute for Theoretical Physics, Astrophysics, Universität Würzburg, Campus Hubland Nord, Würzburg, Germany, Institut für Theoretische Physik, IV Lehrstuhl, Plasma-Astroteilchenphysik, Ruhr-Universität Bochum, Bochum, Germany, INFN Sezione di Roma La Sapienza, Rome, Italy, ILANCE, CNRS-University of Tokyo International Research Laboratory, Kashiwa, Chiba, Japan, Physics Program, Graduate School of Advanced Science, Engineering, Hiroshima University, Hiroshima, Japan, INFN Sezione di Roma Tor Vergata, Rome, Italy, Faculty of Physics, Applied Informatics, University of Lodz, Lodz, Poland, University of Split, FESB, Split, Croatia, Department of Physics, Yamagata University, Yamagata, Japan, Tohoku University, Astronomical Institute, Aobaku, Sendai, Japan, Josip Juraj Strossmayer University of Osijek, Department of Physics, Osijek, Croatia, INFN Dipartimento di Scienze Fisiche e Chimiche-Università degli Studi dell'Aquila, Gran Sasso Science Institute, L'Aquila, Italy, Kitashirakawa Oiwakecho, Kyoto, Japan, Department of Astronomy, University of Geneva, Versoix, Switzerland, Astronomical Institute of the Czech Academy of Sciences, Prague, Czech Republic, Faculty of Science, Ibaraki University, Mito, Ibaraki, Japan, Faculty of Science, Engineering, Waseda University, Shinjuku, Tokyo, Japan, INFN Sezione di Trieste, Università degli Studi di Trieste, Trieste, Italy, INFN, Università degli Studi di Siena, Dipartimento di Scienze Fisiche, della Terra e dell'Ambiente, Sezione di Fisica, Siena, Italy, Escuela Politécnica Superior de Jaén, Universidad de Jaén, Campus Las Lagunillas, Jaén, Spain, Saha Institute of Nuclear Physics, Bidhannagar, Kolkata, India, Institute for Nuclear Research, Nuclear Energy, Bulgarian Academy of Sciences, Sofia, Bulgaria, FZU-Institute of Physics of the Czech Academy of Sciences, Praha, Czech Republic, Dipartimento di Fisica e Chimica 'E. Segrè' Università degli Studi di Palermo, via delle Scienze, Palermo, Gruppo de Electronica, Universidad Complutense de Madrid, Av. Complutense, Madrid, Spain, Department of Applied Physics, University of Zagreb, Zagreb, Croatia, Hiroshima Astrophysical Science Center, Hiroshima University, Higashi-Hiroshima, Hiroshima, Japan, RIKEN, Institute of Physical, Chemical Research, Wako, Saitama, Japan, Charles University, Institute of Particle, Nuclear Physics, Prague, Czech Republic, Division of Physics, Astronomy, Graduate School of Science, Kyoto University, Sakyo-ku, Kyoto, Japan, Institute for Space-Earth Environmental Research, Nagoya University, Chikusa-ku, Nagoya, Japan, Kobayashi-Maskawa Institute, for the Origin of Particles, the Universe, Nagoya University, Chikusa-ku, Nagoya, Japan, Graduate School of Technology, Industrial, Social Sciences, Tokushima University, Tokushima, Japan, INFN Dipartimento di Scienze Fisiche e Chimiche-Università degli Studi dell'Aquila, Gran Sasso Science Institute, L'Aquila, Italy, Department of Physical Sciences, Aoyama Gakuin University, Fuchinobe, Sagami-hara, Kanagawa, Japan, IRFU, CEA, Université Paris-Saclay, Gif-sur-Yvette, France, Graduate School of Science, Engineering, Saitama University, Sakura-ku, Saitama city, Saitama, Japan, Dipartimento di Fisica-Università degli Studi di Torino, Torino, Italy, Department of Physics, Konan University, Kobe, Hyogo, Japan), Heidelberg, Germany, Zeuthen, Germany, CEA Saclay, Orme des Merisiers, Gif-sur-Yvette, and France). Observations of the Crab Nebula and Pulsar with the Large-Sized Telescope Prototype of the Cherenkov Telescope Array. *arXiv e-prints*, art. arXiv:2306.12960, June 2023. doi: 10.48550/arXiv.2306.12960.

[58] F. Di Pierro. Monte Carlo Studies of Combined MAGIC and LST1 Observations. In *36th International Cosmic Ray Conference (ICRC2019)*, volume 36 of *International Cosmic Ray Conference*, page 659, July 2019. doi: 10.22323/1.358.0659.

## Appendix A. Tuning of threshold parameters

The higher light yield of the SiPM devices, as well as the differences in the low-level performance parameters (e.g. pulse width, single phe distribution / afterpulsing) are expected to af-

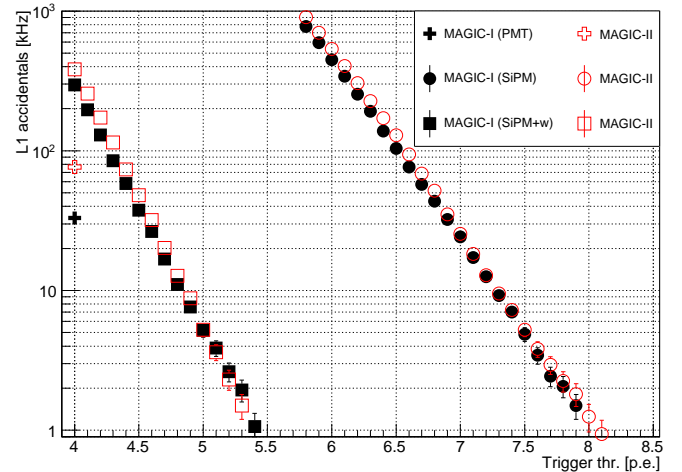


Figure A.11: The expected rate of accidental triggers for SiPM camera (circles) and SiPM with filters camera (squares) as a function of trigger threshold (amplitude in phe) for MAGIC-I (black filled markers) and MAGIC-II (red empty markers). For comparison simulations of PMT-camera at the operational threshold of MAGIC are shown with crosses.

fect the level of the noise induced by NSB. This in turn will determine the operation parameters (threshold), which will have an impact on the achieved low-energy performance. In this appendix we explain the tuning procedure of the simulated trigger threshold parameters and cleaning thresholds in the subsequent analysis

### Appendix A.1. Trigger threshold

In order to determine the optimal trigger thresholds we simulated 100 000 events without Cherenkov photons. For each of them we simulated the response of the telescopes to the NSB within a 160 ns window, and computed number of events producing a single telescope trigger in such a time window. We convert the fraction of triggers  $f_t$  into accidental rate  $r_a$  as  $r_a = f_t / (160 \text{ ns})$  and plot it in Fig. A.11. A similar accidental rate of a SiPM camera without filters requires increase of the thresholds by  $\sim 70\%$ , while with the addition of filters by only  $\sim 12\%$ .

### Appendix A.2. Cleaning threshold

This study is using the standard MARS cleaning, the so-called Sum cleaning with different time and charge thresholds for 2NN (next-neighbour), 3NN and 4NN combinations [48]. The individual NN charge thresholds are normalized to a common cleaning level expressed in phe. With a different level of noise the optimal cleaning level for the analysis might be also affected. To test this we generated and calibrated 20 000 events without Cherenkov photons, with only NSB and electronic noise. Next we applied different cleaning levels, for each of them checking the fraction of events surviving the cleaning. Such a fraction can be interpreted as the maximum fraction of shower events affected by an artificial islands in their image solely due to NSB fluctuations, and thus should be kept low. In the case of PMT simulations the cleaning normalization level of 6 phe results in  $\sim 5\%$  of empty events surviving the cleaning. Fig. A.12 reports the results for SiPM camera without and

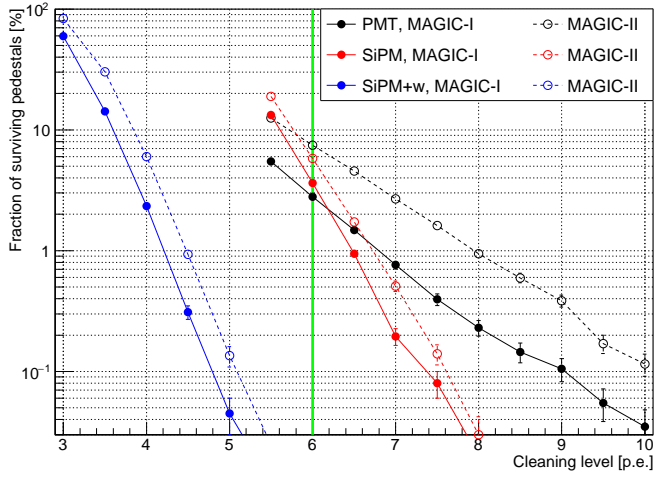


Figure A.12: Fraction of noise-only events surviving image cleaning with a particular cleaning level threshold. SiPM without (red) and with (blue) the wavelength filters is compared with the PMT camera (black). MAGIC-I is shown with filled circles and solid lines, while MAGIC-II with empty circles and dashed lines. Thick vertical green line represent the standard cleaning threshold of PMT camera.

with the filters. The optimal cleaning level for the SiPM camera is similar to the one of PMT camera. With the addition of the wavelength filters instead a factor of 1.5 lower cleaning threshold can be achieved.